Final Report to ONR for the Project "Measurement of Non-Linear Internal Waves and Their Interaction with Surface Waves using Coherent Real Aperture Radars"
ONR Grant N00014-08-1-0977

William J. Plant
Applied Physics Laboratory
University of Washington
March 8, 2010

We operated our coherent microwave radars at sea a total of four times in this project. We operated a radar we call RiverRad on three ships, the R/V Revelle and R/V Ocean Researcher 1 in the South China Sea, and the R/V Endeavor off the coast of New Jersey. In addition, we operated a similar airborne radar, CORAR, on a Cessna Skyhawk off the New Jersey coast at the same time as the Endeavor cruise. A subset of the results from these cruises and flights has been submitted to the Journal of Geophysical Research-Oceans for publication. They have the following titles and are attached to this report:

"The Normalized Radar Cross Section of the Sea for Backscatter: Part 1. Mean Levels"

"The Normalized Radar Cross Section of the Sea for Backscatter: Part 2. Modulation by Internal Waves"

In addition to these two papers, a third paper dealing with our radar measurements of internal wave characteristics in the South China Sea is in preparation and will be submitted shortly. Its title is the following:

"Characteristics of Internal Waves in the South China Sea Observed by Shipboard Radar"

Some of the results presented in these papers can be briefly summarized as follows:

● The multiscale model we developed previously to explain the dependence of the normalized radar cross section (NRCS) of the sea at microwave frequencies on wind speed and direction is viable at VV polarization at much larger incidence angles than we had thought. At this polarization it works out to 89 degree incidence angles. By contrast at HH polarization the model underpredicts the NRCS of the sea for incidence angles above about 45 degrees.

● At high grazing angles, HH polarized cross sections maximize upwind and minimize downwind; upwind they are slightly smaller than VV cross sections . By contrast, at VV polarization cross sections maximize upwind, minimize cross wind, and show a second local maximum downwind, a more standard behavior.

● Generally the NRCS for VV exceeds HH as predicted by theory. However, situations exist on the ocean where HH exceeds VV by as much at 15 dB. These remain unexplained.

REPORT DOCUMENTATION PAGE

1. REPORT DATE (DD-MM-YYYY)	2. REPORT TYPE	3. DATES COVERED (From - To)
08-03-2010	Final Report	1 May 2008 to 31 December 2009

4. TITLE AND SUBTITLE

Final Report to ONR for the Project " Measurement of Non-Linear Internal Waves and Their Interaction with Surface Waves using Coherent Real Aperture Radar

5a. CONTRACT NUMBER

5b. GRANT NUMBER

N00014-08-1-0977

5c. PROGRAM ELEMENT NUMBER

6. AUTHOR(S)

William J. Plant

5d. PROJECT NUMBER

5e. TASK NUMBER

5f. WORK UNIT NUMBER

7. PERFORMING ORGANIZATION NAME(S) AND ADDRESS(ES)

Applied Physics Laboratory - University of Washington
1013 NE 40th Street
Seattle, WA 98105-6698

8. PERFORMING ORGANIZATION REPORT NUMBER

9. SPONSORING/MONITORING AGENCY NAME(S) AND ADDRESS(ES)

Office of Naval Research (ONR 322)
875 North Randolph Street
Arlington, VA 22203-1995

10. SPONSOR/MONITOR'S ACRONYM(S)

ONR

11. SPONSOR/MONITOR'S REPORT NUMBER(S)

12. DISTRIBUTION/AVAILABILITY STATEMENT

Distribution Statement A. Approved for public release; distribution is unlimited

13. SUPPLEMENTARY NOTES

None

14. ABSTRACT

Microwave surface signatures of nonlinear internal waves were investigated in the South China Sea and off the coast of New Jersey in a series of three cruises on US and Taiwanese research vessels and one aircraft flight simultaneous with the cruise off the New Jersey coast. Coherent real aperture radars built by APL/UW were used for these investigations. The results highlighted the role of breaking waves in the formation of these surface signatures and showed that the strain rate of the internal waves controls the location of the surface signature. Shallow water internal waves generally produce surface signatures up to a kilometer in advance of the peak of the wave while in deep water, signatures generally occur directly over the peak. The microwave measurements allowed us to investigate the characteristics of the nonlinear solitons that exist in the South China Sea and their interaction with trains of other smaller, independently travelling internal waves. The soliton speed was found to depend on its amplitude in the manner predicted by two-layer theory.

15. SUBJECT TERMS

internal waves, microwave surface signatures of internal waves, breaking waves, internal wave phase speed

16. SECURITY CLASSIFICATION OF:			17. LIMITATION OF ABSTRACT	18. NUMBER OF PAGES	19a. NAME OF RESPONSIBLE PERSON
a. REPORT	b. ABSTRACT	c. THIS PAGE			William J. Plant
U	U	U	UU		19b. TELEPHONE NUMBER (Include area code) 206-543-7836

Reset

● Internal waves (IW) modulate the mean NRCS to produce maximum cross sections near the IW peak. However the exact location of the maximum varies depending on the strain rate of the IW. For the low strain rates found in deep water, the maximum occurs at the crest while for the larger strain rates often found in shallow water, the maximum occurs well ahead of the crest, sometimes as much as a kilometer.

● Internal waves often cause the HH NRCS to maximize at larger values than the VV NRCS, probably due to breaking wave effects. This calls into question the historical explanation of the effect of IWs on the NRCS, which was based on the modulation of wind waves. Breaking of short gravity waves also appears to be involved.

● The visibility of internal waves in radar imagery appears to vary little with azimuth angle.

● In addition to the large, non-linear solitons that exist in the South China Sea, smaller nearly sinusoidal wave trains also exist that propagate at speeds different than those of the solitons, interact with the solitons, and are modulated by the solitons.

● The solitons travel at speeds that depend on their amplitudes in a manner explained very well by the standard two layer model. These speeds reach 3 m/s in deep water and just over 1 m/s on the shelf.

The Normalized Radar Cross Section of the Sea for Backscatter: Part 1. Mean Levels

William J. Plant, William C. Keller, Kenneth Hayes, Gene Chatham
Applied Physics Laboratory, University of Washington, Seattle, WA, USA
plant@apl.washington.edu

The normalized radar cross section of the sea for backscatter, NRCS or σ_o, is investigated for incidence angles between 0° and 89° using a variety of data collected over more than two decades. For all of these data, the radar return has been compared to that from corner reflectors to yield calibrated normalized radar cross sections. The most recent measurements were made from several ships using a coherent, dual-polarized, X-band radar. These measurements show that σ_o (VV) at high incidence angles exhibits wind speed and azimuth angle dependence similar to those at the lower incidence angles used in scatterometry. It is nearly as large looking downwind as looking upwind and minimizes near the crosswind direction. σ_o(HH) behaves very differently. At incidence angles of 88° to 89°, it is largest looking upwind and smallest looking downwind.

Fits of the multiscale model of microwave backscatter from the ocean (Plant, 2002) to these data along with a variety of data collected previously at lower incidence angles shows that over the whole range of incidence angles from 0° to 89°, σ_o(VV) is rather well explained by the model while measured σ_o(HH) values are generally higher than the model predicts at incidence angles above about 45°. This suggests that scattering phenomena exist on the ocean surface that affect HH backscatter very strongly at the higher incidence angles while impacting VV polarized backscatter only slightly.

This suggestion is strengthened by our observation of high-incidence-angle backscatter from the ocean where σ_o(HH) exceeds σ_o(VV) by as much as 15 dB for long periods of time and over large spatial areas. We examine phenomena that might account for this behavior, including bound, tilted Bragg scatterers, specular points, wedges, spray, and multipath dihedral and cylinderical features. We suggest that multipath dihedral-type features are likely to be relevant scatterers since they produce large σ_o(HH)/σ_o(VV) due to Brewster damping of the first VV bounce.

Introduction

While the normalized radar cross section of the sea, NRCS or σ_o, for cross polarization can be illuminating, for instance in detecting multiple scattering events, it is generally much smaller than copolarized cross sections (Wiltse et al., 1957; Kalmykow and Pustovoytenko, 1976; Lee et al, 1999). For this reason, σ_o values obtained with the electric field of the radiation either vertical σ_o(VV) or horizontal σ_o(HH) on both transmission and reception are more useful modes and ones that have been studied much more than cross polarized cross sections. In this series of two papers we report our work on the copolarized normalized radar cross section of the sea for backscatter, σ_o. The present paper, Part 1, concentrates on the behavior of the mean σ_o as a function of wind speed, incidence angle, and polarization. Part 2 will document our recent measurements on σ_o modulated by surface currents set up by internal waves in the ocean.

Historically σ_o(VV) has been known to be rather well explained by Bragg scattering augmented by a composite, or two-scale, sea surface over the range of incidence angles from approximately 20° to 60° and probably at even higher incidence angles, into the so-called low-grazing angle regime (Wright, 1968; Bass et al., 1968). σ_o(HH), on the other hand, has been, and continues to be, more mysterious. It has appeared to be fairly well predicted by Bragg/composite-surface scattering from 20° to 45° incidence but exceeds the predictions at larger incidence angles. At lower incidence angles, specular scattering has been used to account for both σ_o(VV) and σ_o(HH), but requires an "effective" reflection coefficient. Matching specular and Bragg scattering near 20° incidence is a non-trivial exercise.

In 2002, Plant developed a multiscale model and showed that by adding a third scale of the sea surface and using a Kirchoff integral approach, which is well approximated by Bragg scattering for low wind speeds or moderate to large incidence angles, predictions in agreement with σ_o(VV) and σ_o(HH) measurements could be produced over the incidence angle range 0° to about 45° without invoking an arbitrary effective reflection coefficient (Plant, 2002). Applying the theory beyond this incidence angle range was discouraged in that paper, however, because multiple scattering and breaking waves are not included in the model.

In this paper we show that this multiscale model in fact explains σ_o(VV) over the entire range of incidence angles from 0° to 89° if shadowing is included. σ_o(HH) remains unexplained by the model beyond an incidence angle of about 45°, however. We will investigate possible reasons for this behavior of σ_o(HH), including backscattering from spray and from surface features caused by breaking waves.

Low-Grazing Angle Backscatter from the Ocean

An X-band Doppler radar was operated on the R/V Revelle in the South China Sea in 2005, on the R/V Endeavor off the New Jersey coast in 2006, on the R/V Melville in the Philippine Sea in 2007. The radar transmitted a peak power of 10 watts and used a pulse width of 15 m in 2005, 3.75 m in 2006, and 30 m in 2007. The radar is the RiverRad system that was developed for river surface velocity measurements and is described more fully in Plant et al., 2005. It is shown mounted on the three ships in Figure 1.

In all three years, we calibrated the sea return against that from a corner reflector so that fully calibrated normalized radar cross sections, σ_o, could be obtained. In 2005, only VV polarized backscatter was obtained due to a switch failure and the antennas were fixed looking nearly toward the bow of the ship. In 2006, both HH and VV backscatter were collected. The antennas scanned through approximately 80° and were directed 35° apart in azimuth. In 2007, the antennas were again fixed but this time looking perpendicular to the heading of the ship; both HH and VV backscatter were collected. On all cruises, backscatter was collected both from seas disturbed only by the wind and from seas where internal waves were present.

Figure 1. RiverRad mounted on the ships. a) R/V Revelle in 2005, b) R/V Endeavor in 2006, c) R/V Melville in 2007.

Figure 2 shows the angular dependence of σ_o(VV) observed in 2005 at an 89° incidence angle and at various wind speeds in the absence of internal waves. Note that σ_o(VV) exhibits the same second-harmonic dependence on azimuth angle that it does at lower incidence angles. This is not the case for the horizontally polarized cross section, σ_o(HH) shown in Figure 3 at nearly the same incidence angle. Here both σ_o(VV) and σ_o(HH) are shown as determined from the measurements of 2006. σ_o(HH) maximizes when the antenna looks into the wind and minimizes in the opposite direction. These results agree with the uncalibrated, nearshore measurements of Trizna and Carlson, 1996.

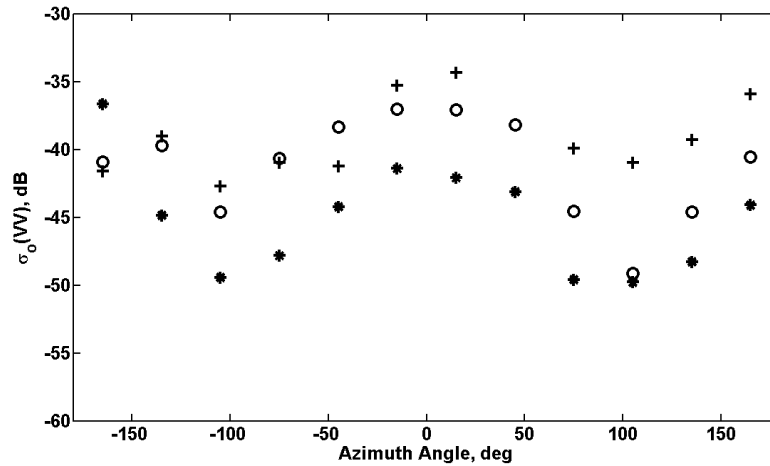Figure 2. Angular dependence of σ_o(VV) at X-band and an incidence angle of $89^{o\ +-}$ 0.25^o. These 2005 results are for the ocean surface disturbed only by wind. Symbols are for various wind speeds: $+ = 4$ m/s, o $= 6$ m/s, $+ = 8$ m/s.
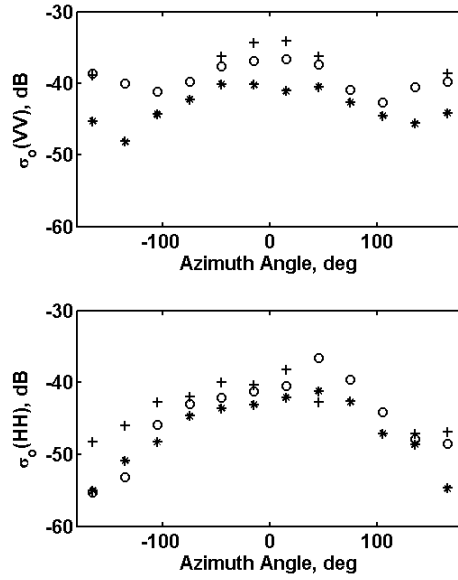
Figure 3. a. Angular dependence of $\sigma_o(VV)$. b. Angular dependence of $\sigma_o(HH)$. These 2006 results are for a sea surface disturbed only by wind; the incidence angle is $88.3^{o\ +-}\ 0.1^o$. Symbols as in Figure 2.

Figures 4 and 5 show the wind speed dependences of these data and compare them to simple Bragg scattering predictions using the spectrum of Elfouhaily et al., 1997. Clearly the Bragg predictions are much too low and the increase with wind speed is too small. In fact, Bragg predictions for $\sigma_o(HH)$ are below the bottom of the plot in Figure 5b.
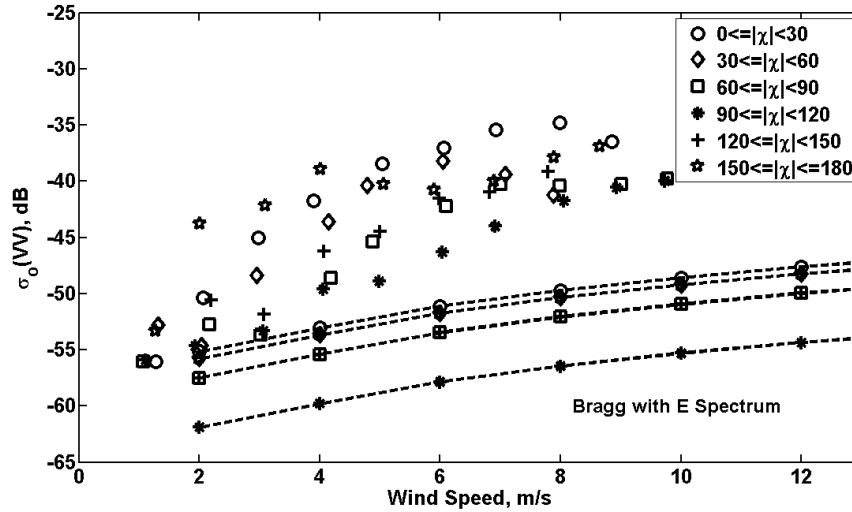

Figure 4. Wind speed dependence of $\sigma_o(VV)$ at various azimuth angles from the wind for the data of 2005. χ is the angle between the antenna look direction and the direction from which the wind comes. Lines show simple Bragg scattering predictions using the wind wave spectrum of Elfouhaily et al., 1997.
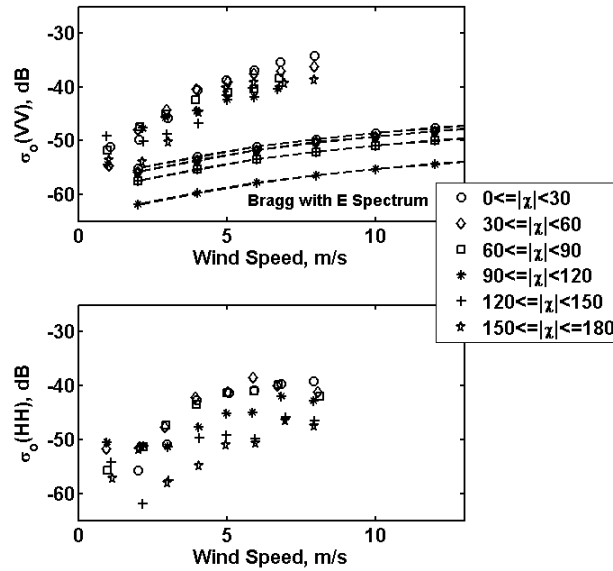
Figure 5. Wind speed dependence of σ_o at various azimuth angles from the wind for the data of 2006. a. σ_o(VV), b. σ_o(HH). Lines show simple Bragg scattering predictions for σ_o(VV) using the wind wave spectrum of Elfouhaily et al., 1997; σ_o(HH) predicted by Bragg scattering is below the bottom of the lower graph.

This under prediction can be overcome for σ_o(VV) by resorting to the multiscale model (Plant 2002). This model extended the standard composite surface model to include effects of waves that were intermediate between Bragg scattering waves and long, modulating waves. This model used results of the small slope approximation (Voronovich, 1985) and the integral expansion method (Fung et al, 1992) for backscatter to combine specular and Bragg scattering into a single Kirchhoff integral that covered incidence angles from nadir to mid-range. The predictions of this model were shown to agree well with the Ku-band airship data mentioned above and with other data sets at C and Ka bands as well as Ku-band at nadir incidence. These comparisons, however, were only done for incidence angles up to 50° because breaking waves and spray were not included in the model, making it questionable above this incidence angle.

The improved fit using this model is demonstrated in Figure 6 where the left panels show σ_o(VV) versus wind speed for upwind, downwind, and crosswind looks. The squares in this figure are results of the multiscale model modified to include simple geometric shadowing. Intermediate-scale facets were not included in the calculations if they could not be seen by the antenna. Bragg scattering predictions can also fit the data if a mean tilt of the illuminated parts of the surface given by U/4 is assumed, where tilt is in degrees and U is in m/s. This yields the red lines in Figure 6

Figure 6 also shows similar data and models for σ_o(HH) in the right panels. Here the measured values are much larger than either those predicted by the multiscale model or by tilted Bragg. This is true even when the antenna is directed down wind and wave. Since breaking wave effects are generally assumed to have little effect on backscatter

with the antenna directed nearly down wave, we interpret these results to mean that a scattering mechanism exists at these grazing angles other than multiple scattering from breaking waves that affects σ_o(HH) much more than σ_o(VV). This is reasonable considering the much higher level of σ_o(VV) shown in the downwind part of Figures 3 and 5. Thus we need an increase in the σ_o(HH) values predicted by the multiscale model of about 10 dB in the downwind direction and about 20 dB in the upwind direction in order to explain the data.
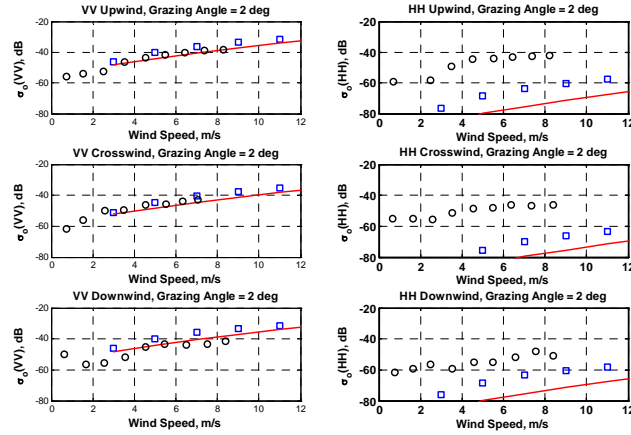

Figure 6. Fit of the multiscale model (squares) to the data of 2006 for upwind looks (circles). The red lines are Bragg scattering predictions if the local grazing angle in degrees is larger than the nominal one by U/4, where U is wind speed in m/s.

Fits to the Multiscale Model over all Incidence Angles

To check the predictions of the multiscale model further, we compared it with lower incidence data in addition to these high-incidence-angle measurements. Over the last two decades, we have collected a variety of σ_o(VV) and σ_o(HH) data at 14.0 GHz (Ku-band) and 9.36 GHz (X-band). These data were collected at many different incidence angles, wind speeds, and azimuth angles from platforms as varied as research platforms, airships, airplanes, and ships (Plant, 1997; Plant et al., 1998,2005).

Figures 7-10 show the comparison out to higher incidence angles that shown in Plant (2002). The predictions of the multiscale model for σ_o(VV) and σ_o(HH) are compared with the following data sets: Ku-band collected on the German Research Platform Nordsee (Plant 1997, 2003b), on the airship off the coast of Oregon (Plant et al., 1998), and the TOPEX/Poseidon satellite altimeter (Hwang, 1998); X-band data from a Twin Otter aircraft flown off the coast of North Carolina (Plant et al.,2005) and the ship data discussed above. We ran the model with various ocean wave spectra and for both X and Ku band. Figures 7-10 show the results for the spectrum that Plant (2002) calls the D-spectrum, a combination of spectra suggested by Donelan, Banner, and Plant. Comparisons of predictions with other spectral models can change the model predictions somewhat.

Figures 7-10 show predictions of the multiscale model at both Ku and X-bands. They are very similar above the lowest wind speed, differing by 3 dB at most for a 4 m/s wind speed. The data at wind speeds of 8 (Figure 8), 12 (Figure 9) and 16 m/s (Figure 10) all indicate that the model predicts $\sigma_o(VV)$ rather well over the whole range of incidence angles from 0° to 89° for upwind, crosswind, and downwind antenna look directions. At 4 m/s (Figure 7), the fit is less good in places but wave spectra at this wind speed can vary widely due to wind variability (Plant, 2000). The fit is not as good for $\sigma_o(HH)$. For this polarization, the predictions appear to be accurate up to an incidence angle of about 45° but fall significantly below the data for higher incidence angles. This is true for all three antenna look directions. In a following section, we will discuss possible reasons that the multiscale model might under predict $\sigma_o(HH)$ at high incidence angles.
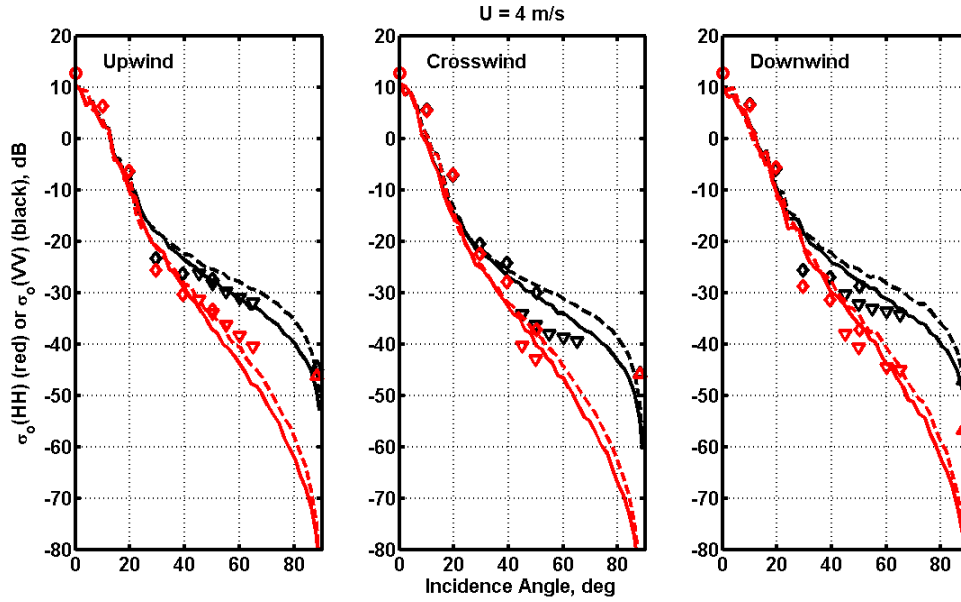
Figure 7. Comparison of predictions of the multiscale model with data for a wind speed of 4 m/s. The D-Spectrum of Plant (2002) was used in the calculation. Black lines are predictions at Ku-band while dashed lines are predictions at X-band. Red always indicates $\sigma_o(HH)$ while black is $\sigma_o(VV)$. Symbols for data are as follows: circles – Ku-band data from the TOPEX/Poseiden altimeter; diamonds – Ku-band from the airship (Plant et al., 1998); down triangles – X-band from the airplane (Plant et al., 2005); up triangles – X-band data from the ships discussed above.

Figure 8. Same as Figure 7 but for a wind speed of 8 m/s. The squares are Ku-band data from the Nordsee platform (Plant, 1997, 2003b)

Figure 9. Same as Figures 7 and 8 but for a wind speed of 12 m/s.

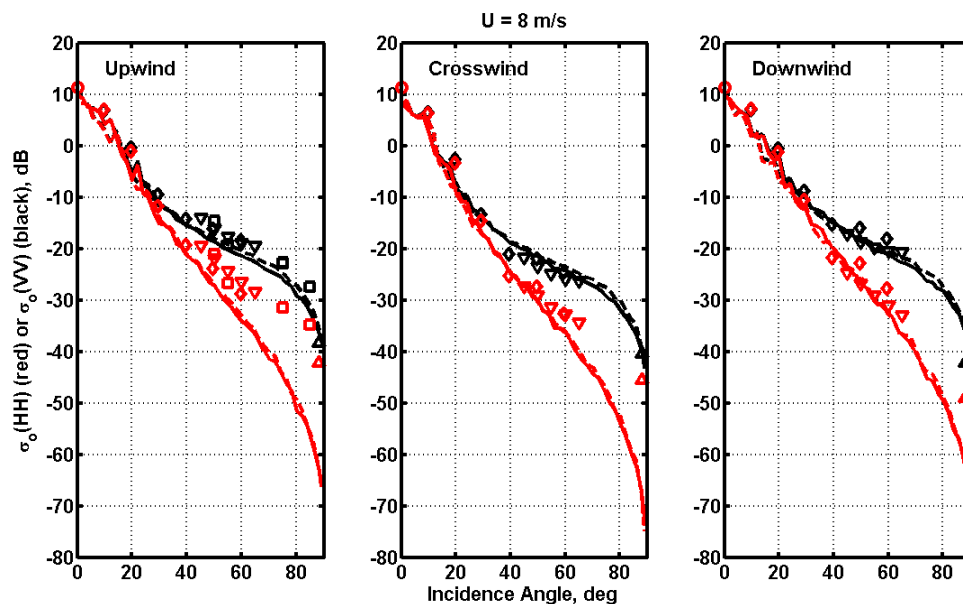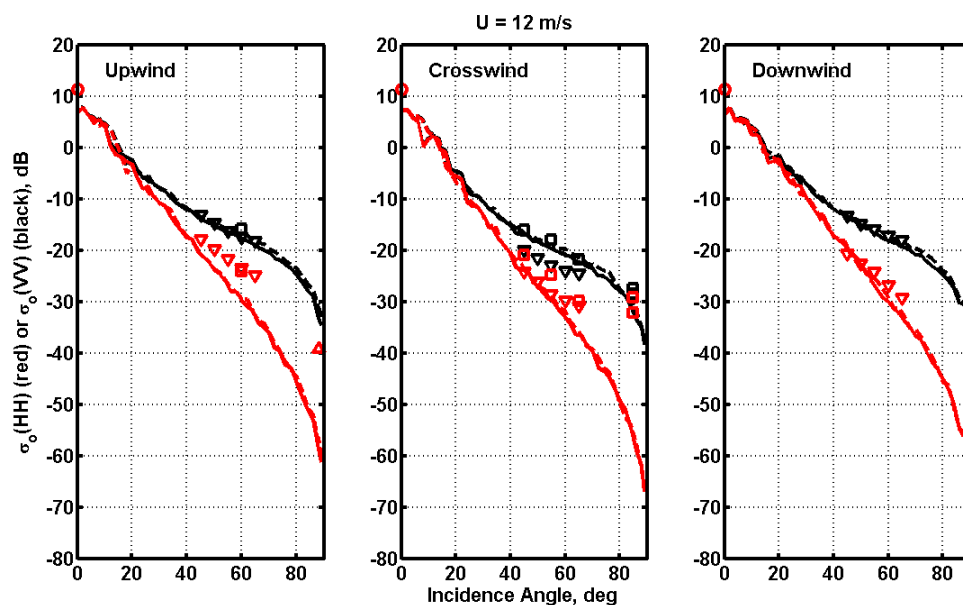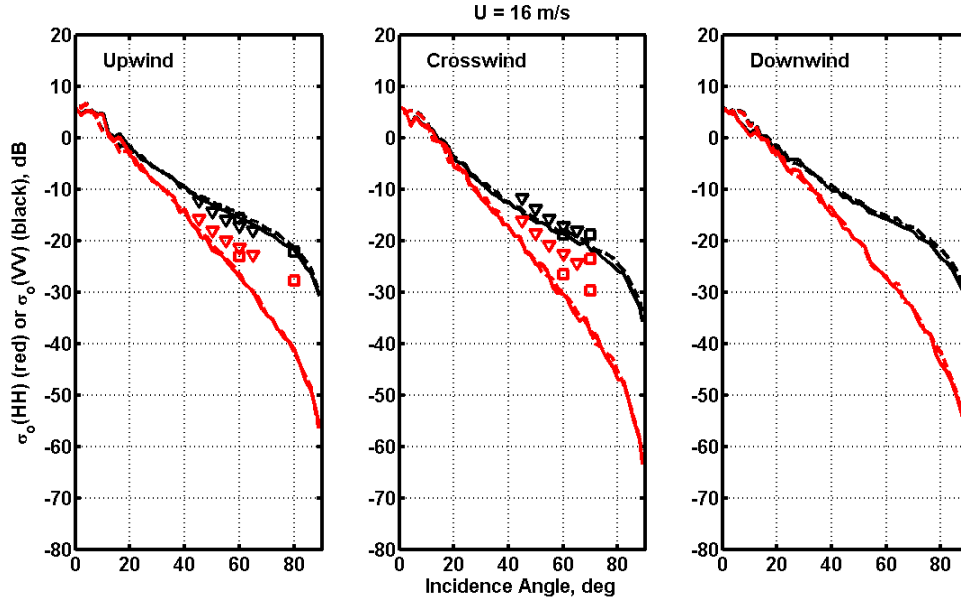Figure 10. Same as Figures 7 and 8 but for a wind speed of 16 m/s.

Anomalous Low-Grazing Angle Backscatter from the Ocean

In Part 2 of this paper, we will show that internal waves can sometimes generate surface conditions for which $\sigma_o(HH) > \sigma_o(VV)$, which as shown above does not normally occur for ocean backscatter on large scales. However, we have observed an occurrence of mean $\sigma_o(HH)$ larger than mean $\sigma_o(VV)$ in 2007 when the RiverRad operated from the R/V Melville around the Philippine Islands. In the images collected, we observed many regions of high oceanic backscatter of unknown cause. An example is shown in Figure 11. A total of 15 images of similar quality were collected. The figure shows $\sigma_o(HH)$ and $\sigma_o(VV)$ in dB with associated scatterer velocities in m/s. Also shown in the bottom panel of the figure are the wind speed, wind direction, ship speed, and ship heading. The antennas looked broadside to the ship on the starboard side and were 16.5 m above the water. The high cross section and velocity features cover more than 2 km in range and lasts for nearly 5 minutes as the ship goes by at 6 m/s. Thus the features are also about 2 km in the azimuth direction. $\sigma_o(HH)$ is 5 to 15 dB larger than $\sigma_o(VV)$ over most of this region.

The large regions covered by this anomalous backscatter lead us to believe that it is not of man-made origin, for instance interference from other marine radars. This belief is strengthened by the fact that most of the high-backscatter regions occur near the ship at the same time that shifts in wind speed or direction were measured by the ship's anemometer. We cannot rule out the involvement of rainfall in the occurrence of these features since precipitation measurements on the ship were not adequate to examine this possibility. In any case, it seems obvious that these features are a natural phenomenon associated with low-grazing angle backscatter from the sea surface.
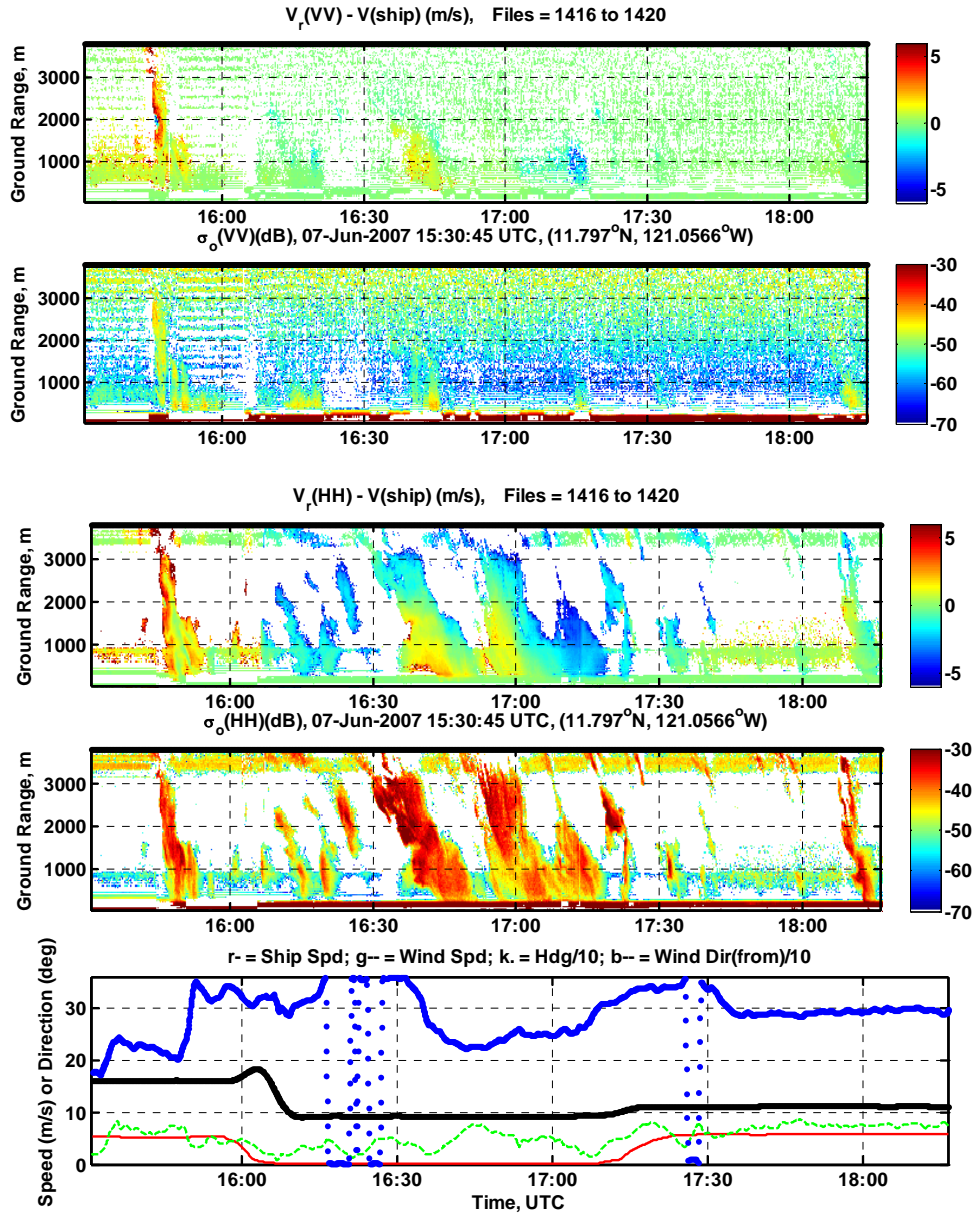
Figure 11. Space/time images of σ_o(HH) and σ_o(VV) along with their associated velocities. Note the dramatically larger cross section and velocities for HH polarization inside the pronounced features. The bottom panel shows ship and wind parameters.

To document this farther, and to assure that these results are not a product of faulty radar calibration, we show time series of σ_o(HH) and σ_o(VV) at an incidence angle of 88.75° for two different time periods near the Philippine Islands in Figure 12. This incidence angle was chosen because it corresponds to the center of the beam from the two-foot-diameter parabolic antennas that were used to collect these data. This angle therefore corresponds to the largest signal-to-noise ratio. One of the time periods shown in Figure 12 corresponds to the image of Figure 11 while the other was obtained well

away from any such anomalous backscattering features. Clearly σ_o(HH) is smaller than σ_o(VV) when the ocean surface is disturbed only by the wind but becomes larger than σ_o(VV) in the anomalous region.

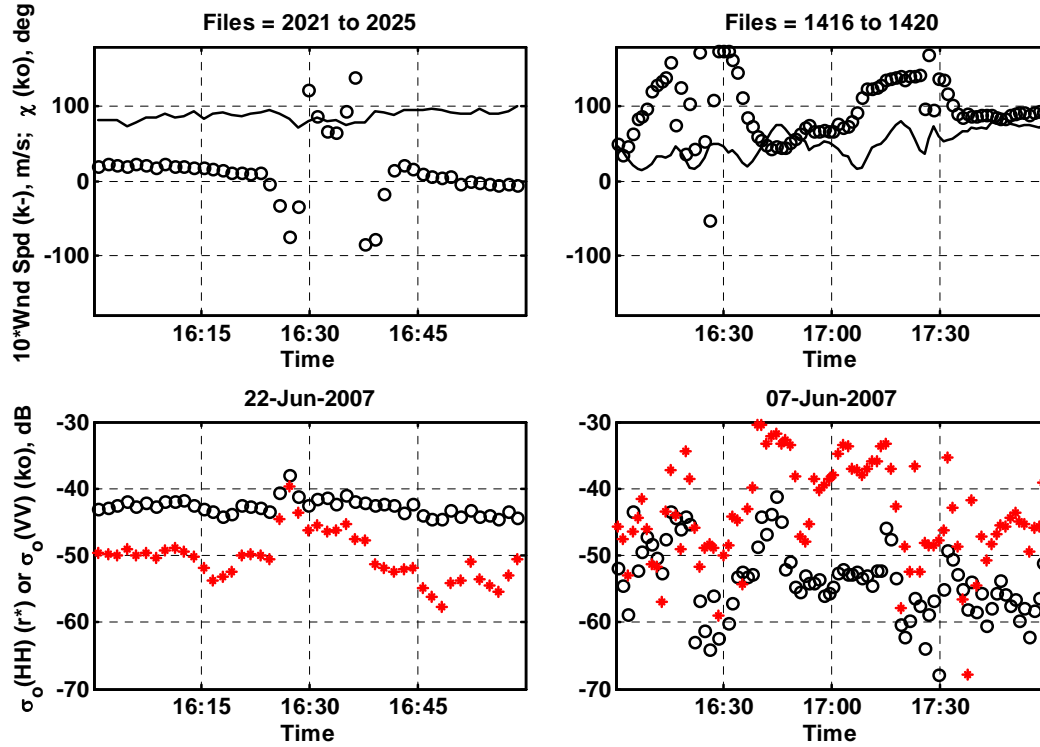Figure 12. Documentation of variable polarization ratios at an incidence angle of 88.75° +- 0.25°. Top row: Solid line is 10 times the wind speed, circles are azimuth angle with respect to the direction from which the wind comes, χ. Bottom row: Measured σ_o(HH) (red asterisks) and σ_o(VV) (black circles) at the times of the plots in the top row.

Clearly Bragg scattering cannot account for these features. In the next section, we explore some ideas that have been put forward to explain these non-Bragg features and take the first steps toward a method for including the most important ones in the model.

Other Scattering Mechanisms

The fact that the multiscale model does not predict the large values of σ_o(HH) that are observed at incidence angles above 45° in all look direction suggests that scattering processes other than the Bragg scattering processes described by the standard composite surface theory may be occurring at high incidence angles. This has been noted many times in the past by a variety of authors (See Churyumov et al., 2002, for instance). In fact, the data suggest that more than one of these non-standard scattering mechanisms may be at work. As discussed further below, many of the non-Bragg processes that have been proposed over the years involve breaking waves; Bragg scattering from bound, tilted waves proposed by Plant (1997) also require breaking, or at least crumpling, waves. However, the fact that σ_o(HH) is higher than predicted in the downwind look direction (See Figures 6-8) is difficult to explain using only a mechanism tied to breaking waves.

Such wave-breaking regions exist primarily near wave crests or on the front face of waves and their effects should be much weaker when the antenna is looking downwind, especially at very high incidence angles.

Many possibilities for the additional backscatter at HH polarization have been proposed over the years. These include bound, tilted waves due to the breaking of short gravity waves, specular backscatter, wedges, spray, and multipath scattering from steep features.

Plant (1997) proposed that some features of HH backscatter at incidence angles greater than 45° can be explained by Bragg scattering but from the rough patches produced by breaking short gravity waves that travel with the the gravity waves rather than from freely propagating centimetric surface waves. In particular, observations of larger Doppler shifts in HH than in VV backscatter and of low coherence between HH Doppler shifts and dominant ocean wave orbital velocities when looking into the wind at large incidence angles can be explained. The patches are assumed to be strongly tilted toward the antenna under these conditions and this tilt increases HH Bragg scattering more than VV. The existence of bound, tilted waves in wind-generated and breaking wave systems has been well substantiated by wave tank experiments (Plant et al., 1999a, 1999b, 2004; Rozenberg et al., 1999; Lee et al., 1999). The skewness of sea surface slope probability distributions can also be explained on the basis of such waves (Plant, 2003a). Nevertheless, bound, tilted waves do not seem to account for all of the excess backscatter (over standard Bragg/composite) for HH polarization at high incidence angles. Bragg scattering from bound, tilted waves cannot account for large $\sigma_o(HH)/\sigma_o(VV)$ ratios except momentarily (Plant, 2003b). It also cannot account for $\sigma_o(HH)$ being too large in the downwind look direction. Furthermore, a limit exists on how strong the scattering from bound, tilted waves can be since their effects are not observed in VV backscatter. This limit is sufficiently low to ensure that bound, tilted waves cannot explain all of the excess backscatter even in the upwind direction.

Specular backscatter has frequently been invoked as a means for increasing the $\sigma_o(HH)/\sigma_o(VV)$ polarization ratio at large incidence angles (Chubb,1999; Kudryatzev, 2005). While the assumption that sufficient specular points exist nearly perpendicular to the high-incidence-angle incident field to produce significant backscatter is arguable, this mechanism clearly cannot produce polarization ratios much larger than one, as observed above.

Wedge scattering, which is scattering from sharp crests of significant extent in the horizontal, has been suggested as a means of increasing high-incidence angle backscatter at HH polarization (Lyzenga et al., 1983). Previous work on backscatter from these structures had been contradictory. Kalmykov and Pustovoytenko (1976) suggested that it produced a polarization ratio greater than one at high incidence angles while Lewis and Olin (1980) said it produced polarization ratios less than one. Lyzenga et al. showed that the polarization ratio was above one at incidence angles higher than a level set by the wedge angle and below one for lower incidence angles. Thus, while these structures may contribute somewhat to the backscatter, they cannot explain our observations of $\sigma_o(HH)/\sigma_o(VV) > 1$ at very high incidence angles.

One exception to this statement is for incident radiation that is strikes the wedge from above, that is, perpendicular to its base. This configuration is most likely to occur for high incidence angles when the "wedge" is the tip of a plunging breaking wave.

Churyumov et al. (2002) showed that under these conditions the backscatter may have a polarization ratio above one. Three-dimensional numerical calculations by Li and West, (2006) indicated the same phenomenon. The density of plunging breakers on the open ocean is likely to be rather low under normal conditions, however, so this mechanism may contribute relatively little to the mean backscatter in most cases.

Spray above the water surface that is produced by actively breaking waves is another possible source of backscatter. Bounces from the surface of the water to the spray droplets will serve to augment the direct backscatter from the drops. Both this and possible flattening of the drops could produce HH backscatter that is larger than VV backscatter. However, Plant (2003b) showed that if spray is to account for the increased backscatter at HH polarization and high incidence angles, it must increase with wind speed much more slowly than is generally observed. On the other hand, Plant et al. (2006) later showed that while large Doppler shifts due to backscatter from spray can be observed in a wind wave tank, the spray responsible for the backscatter is located too close to the surface to be measured with in situ instruments. Thus the question of the role of spray in high-incidence backscatter is still open.

Multipath scattering from steep surface features is perhaps the most likely source of this observation. Backscatter from breaking waves has been studied for many years and clearly shows that $\sigma_o(HH)$ can exceed $\sigma_o(VV)$ during breaking (Lee et al, 1998; Fuchs et al., 1999; Sletten et al., 2003) . Most researchers have invoked some type of multiple scattering phenomena to explain this behavior (Wetzel, 1986; Trizna, 1997; Holliday et al., 1998; West, 1999, 2002; Lee et al, 1997, 1998). Wetzel (1986) seems to have been the first to suggest the importance of this type of scattering. He proposed that the backscatter resulted from a bounce of the incoming ray from the water surface in front of a bore-like front resulting from breaking. He modeled this as a quarter cylinder rising out of a flat, tilted sea surface and multiplied the standard cylinder cross section by a "proximity factor" to account for the presence of the flat surface. His results, while including Brewster damping of vertically polarized rays at the first bounce, indicate that VV backscatter will be stronger than HH backscatter for large incidence angles.

Lee et al. (1997) and Trizna (1997) both proposed that the structures producing backscatter during breaking could be better modeled by a dihedral in which two water surfaces at right angles produce a double-bounce backscatter. Both suggested that Brewster damping of VV polarized incident radiation at the initial bounce would reduce its backscatter level compared to that of HH polarization. Lee et al. carried out experiments that verified this. Trizna concentrated on the interference of the ray directly incident on the vertical surface and that reflected from the horizontal surface. Since both of these rays cannot be reflected to the antenna simultaneously, however, it is unclear why this interference is a concern.

While dihedrals are clearly idealized scattering structures, numerical studies show that similar multiple scattering phenomena occur for a breaking wave at and immediately after breaking (West,1999, 2002; Fuchs et al., 1999). These studies also show that the exact nature of this multiple scattering depends critically on the shape of the surface (Lee et al, 1998; Fuchs et al., 1999; West, 2002; Sletten et al.,2003). Furthermore, multiple scattering also occurs for strong breaking in the very turbulent region produced by breaking, as evidenced by the cross polarized signal and $\sigma_o(HH)$ greater than $\sigma_o(VV)$ (Lee et al., 1998). Therefore, a statistical model of backscatter from breaking waves in

which the scattering is due to multiple scattering from randomly oriented dihedrals has been proposed (Lee et al., 1998) and may not be a bad approximation to reality.

Water Dihedrals

As a first step in this procedure, we calculate the backscattering cross section of dihedrals formed by two perpendicular water surfaces. The geometry is sketched in Figure 13. We will take a geometric optics approach and ignore diffraction except insofar as it enters into the determination of the cross section. Thus, we consider only incident and backscattered rays lying in the plane of incidence as shown in Figure 12. We will let the electric field vector lie at an angle φ to the plane of incidence.
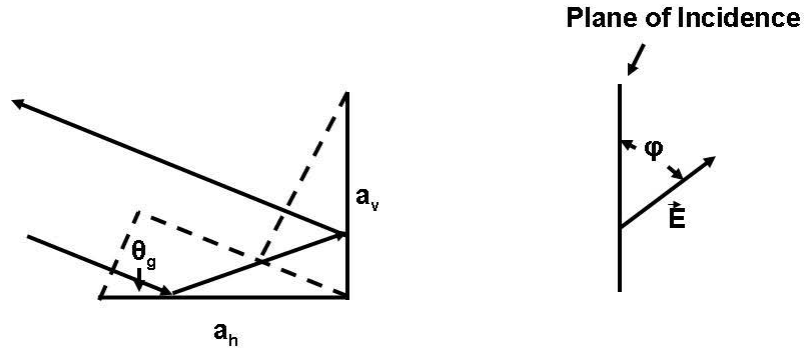

Figure 13. Diagram of the dihedral scattering geometry. Sides of the dihedral are a_v and a_h, θ_g is the grazing angle, and the electric field **E** makes an angle φ with the plane of incidence.

As usual for simple targets, the cross section σ is given by

$$\sigma = A_p|R|^2D \tag{1}$$

where Ap is the projected area, R is the reflectivity, and D is the directivity. We will let the width of the dihedral by b. Then

$$A_p = b(a_1\sin\theta_g + a_2\cos\theta_g), \qquad a_1 = \min(a_h,a_v\cot\theta_g); a_2 = \min(a_v,a_h\tan\theta_g)$$
$$R = [R_v(\theta_g)\exp(-i\pi/2)\cos\varphi + R_h(\theta_g)\sin\varphi][R_v(\pi/2-\theta_g)\exp(-i\pi/2)\cos\varphi + R_h(\pi/2-\theta_g)\sin\varphi] \tag{2}$$
$$D = 4\pi A_p/\lambda^2$$

where Rv and Rh are Fresnel reflection coefficients for vertical and horizontal polarization, respectively, λ is microwave length, and a_v and a_h are the lengths of the vertical and horizontal planes of the dihedral. The factor $\exp(-i\pi/2)$ in the reflectivity accounts for the fact that R_v is a ratio of magnetic fields while R_h is a ratio of electric fields. For perfect reflectivity, $R_v = 1$ and $R_h = -1$ so the maximum cross section at $\theta_g = 45^o$ with $a_h = a_2 = a$ is

$$\sigma_{max} = 8\pi a^2b^2/\lambda^2 \tag{3}$$

as required. The cross section for a water dihedral at X-band ($\lambda = 3$ cm) is plotted versus grazing angle in Figure 14 for b = 1 cm and various values of a. To produce these curves, Eq.(1) has been convolved with a spreading function corresponding to the vertical beamwidth of the vertical plate:

$$f(\theta_g) = \exp\{-[4 \ln 2\ \theta_g^2\ a_v^2/\lambda^2]\}/N \qquad (4)$$

where N is a normalizing factor to make the integral of f over θ_g be one.
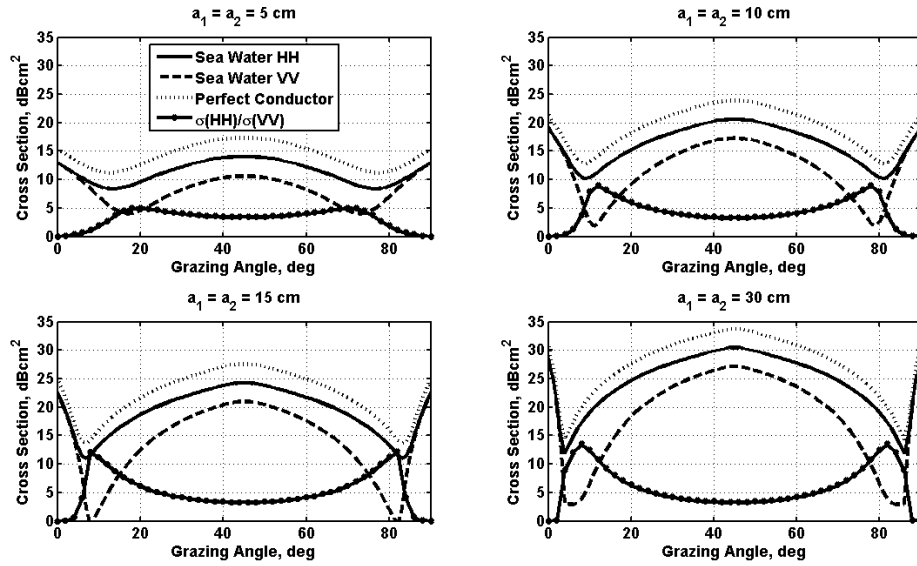

Figure 14. Cross sections of dihedral corner reflectors of various sizes as a function grazing angle. The curves with diamonds are HH/VV polarization ratios in dB. The width of the dihedral is 1 cm. a_1 is the length of the horizontal plane while a_2 is the length of the vertical plane.

Several features of these plots are of interest. First, while the cross sections obviously increase with dihedral size at 45°, this is not true at the grazing angles of more interest to sea clutter. In particular, for grazing or incidence angles near 5°, cross sections do not monotonically increase with dihedral size. Nevertheless, these levels alone do not determine the magnitudes of backscattering cross sections since the temporal and spatial densities of the dihedrals will also affect the values. Second, peaks of the cross sections at 0° and 90° grazing angles are due to specular reflections from the vertical and horizontal planes of the dihedrals, respectively. They will clearly affect cross sections not only near grazing but also near nadir. The nadir cross sections may limit the densities of these types of scatterers that we can choose since backscattering at nadir is well understood. Third, note that the HH/VV polarization ratio is greater than one only at grazing angles above a few degrees. Since this is often higher than the nominal grazing angles used, for instance, from ships, observations of the polarization ratios will be affected by the tilting of the dihedrals by the long waves on which they ride. Finally, note that for grazing angles between about 5° and 20°, the polarization ratio increases with dihedral size. This effect will not be changed by summing over many such features. Thus we suspect that larger observed polarization ratios will correspond to larger dihedral features on the surface and therefore to more energetic breaking events.

Conclusion

Measurements of the mean normalized radar cross section of the sea taken over many years, from many different platforms, and at many different incidence angles have shed light on possible backscattering mechanisms of the ocean surface. The measurements show that $\sigma_o(VV)$ for a sea surface disturbed only by wind is generally well explained by the multiscale model (Plant, 2002) over the entire range of incidence angles from 0° to 89°. This model is simply a slightly modified version of the standard composite surface theory of Wright (1968) and Bass et al. (1968). $\sigma_o(HH)$, on the other hand, begins to be higher than predicted by this model at incidence angles above about 45° but remains below $\sigma_o(VV)$ under normal conditions. While at very high incidence angles, both cross sections increase with wind speed as in standard scatterometry and $\sigma_o(VV)$ displays the standard second-harmonic dependence on azimuth angle, $\sigma_o(HH)$ shows a very different azimuth angle dependence. It is highest looking into the wind and lowest looking downwind. In both cases the magnitude of $\sigma_o(HH)$ is larger than expected from the multiscale model.

Observations of anomalous backscatter from the ocean that depart from this model have been obtained in the Philippine Sea. While the cause of this anomalous backscatter is unknown, it clearly shows that $\sigma_o(HH)$ can at times exceed $\sigma_o(VV)$ over large time and space scales for low-grazing-angle backscatter from the ocean. Taken together, these observations show that other scatterers besides short wind-driven waves exist on the ocean surface. Several different types of these scatterers probably exist. They include bound, tilted waves from "crumpling" short gravity waves, jets from plunging breaking waves, spray, and multipath surfaces most conveniently described as water dihedrals. These types of scatterers begin to manifest themselves when their normalized radar cross section exceeds the standard Bragg scattering from wind waves. This most commonly occurs for HH polarization at high incidence angles but may also be caused or exaggerated by anomalous conditions such as shear currents as we will show in Part 2.

Since multipath surfaces are likely to be the dominant types of these other scatterers at very high incidence angles, we derived a geometrical optics expression for their cross section versus grazing angle. This showed that such dihedrals must be tilted up toward the incoming signal in order to produce $\sigma_o(HH)/\sigma_o(VV)$ polarization ratios that exceed one. Still to be determined are the distribution of orientations of the dihedrals and their density on the ocean surface under different circumstances. A limitation on these variables will be the known density of specular scatterers at nadir.

Acknowledgments

References

Bass, F.G., I.M. Fuks, A.I. Kalmykov, I.E. Ostrovsky, and A.D. Rosenberg, Very high frequency radiowave scattering by a disturbed sea surface. Part II: Scattering from an actual sea surface. IEEE Trans. Antenna and Propagation, AP-16(5), 560-568, 1968.

Chubb, S.R., A. L. Cooper, R. W. Jansen, R. A. Fusina, J-S Lee, and F. Askari, Radar Backscatter from Breaking Waves in Gulf Stream Current Convergence Fronts, IEEE Trans. Geosci. Rem. Sensing, 37(4), 1951-1966, 1999.

Churyumov, A.N., YU.A. Kravtsov, O.YU. Lavrova, K. TS. Litovchenko, M.I. Mityagina, and K. D. Sabinin, Signatures of resonant and non-resonant scattering mechanisms on radar images of internal waves, Int. J. Remote Sensing, 23(20), 4341-4353, 2002.

Cox, C., and W. Munk, Statistics of the sea surface derived from sun glitter, J. Mar. Res., 13(2), 199–227, 1954.

Fung, A.K., Z. Li, and K.S. Chen, Backscattering from a randomly rough dielectric surface, IEEE Trans on Geosci. and Rem. Sensing, 30, 356-369, 1992.

Holliday, D., L.L. DeRaad, Jr., and G.J. St-Cyr, Sea-spike backscatter from a steepening wave, IEEE Trans. Ant. Prop., 46(1), 108-113, 1998.

Hwang, P.A., W.J. Teague, G.A. Jacobs, and D.W. Wang, A statistical comparison of wind speed, wave height, and wave period derived from satellite altimeters and ocean buoys in the Gulf of Mexico region, J. Geophys. Res., 103(C5), 10451-10468, 1998.

Kalmykow, A.I., and V.V. Pustovoytenko, On polarization features of radio signals scattered from the sea surface at small grazing angles, J. Geophys. Res., 81(12), 1960-1964, 1976.

Kudryavtsev,V., D. Akimov, J. Johannessen, and B. Chapron, On radar imaging of current features: 1. Model and comparison with observations, J. Geophys. Res., 110, C07016, doi:10.1029/2004JC002505, 2005.

Lee, P.H.Y., J.D. Barter, K.L. Beach, C.L. Hindman, B.M. Lake, H. Rungaldier, H.R. Thompson Jr., and R. Yee, Experiments on Bragg and non-Bragg scattering using single-frequency and chirped radars, Radio Science, 32(5), 1725-1744, 1997.

Lee, P.H.Y., J.D. Barter, K.L. Beach, B.M. Lake, H. Rungaldier, H.R. Thompson Jr., and R. Yee, Scattering from breaking gravity waves without wind, IEEE Trans. Ant. Prop., 46(1), 14-26, 1998.

Lee, P.H.Y., J.D. Barter, K.L. Beach, B.M. Lake, H. Rungaldier, H.R. Thompson Jr., L. Wang, and R. Yee, What are the mechanisms for non-Bragg scattering from water waves?, Radio Sci., 34(1), 123-138, 1999.

Lewis, B.L. and I.D. Olin, Experimental study and theoretical model of high resolution backscatter from the sea, Radio Sci., 15, 815-826, 1980.

Lyzenga, D.R., A.L. Maffett, and R.A. Shuchman, The contribution of wedge scattering to the radar cross section of the ocean surface, IEEE Trans. Geosci. Rem. Sens., 21(4), 502-505, 1983.

Plant, W.J., A model for microwave Doppler sea return at high incidence angles: Bragg scattering from bound, tilted waves, J. Geophys. Res, 102(C9), 21131-21146, 1997.

Plant, W.J., Effects of wind variability on scatterometry at low wind speeds, J. Geophys. Res., 105(C7), 16899-16910, 2000.

Plant, W.J., A new interpretation of sea-surface slope probability density functions, J. Geophys. Res, 108(C9), 3295, doi:10.1029/2003JC001870, 2003a.

Plant, W.J., Microwave sea return at moderate to high incidence angles, Waves in Random Media, 13(4), 339-354, doi: 10.1088/0959-7174/13/4/009, 2003b.

Plant, W.J., W.C. Keller, V. Hesany, and K. Hayes, Measurements of the marine boundary layer from an airship, J. Atmos. Ocean. Tech., 15, p.1433-1458, 1998.

Plant, W.J., W.C. Keller, V. Hesany, T. Hara, E. Bock, and M. Donelan, Bound waves and Bragg scattering in a wind wavetank, J. Geophys. Res., 104(C2), 3243-3263, 1999a.

Plant, W.J., P.H. Dahl, and W.C. Keller, Microwave and acoustic scattering from parasitic capillary waves, 1999. J. Geophys. Res., 104(11), 25,853-25,866, 1999b.

Plant, W.J., A stochastic, multiscale model of microwave backscatter from the ocean, J. Geophys. Res.,107(C9), 3120, doi:10.1029/2001JC000909, 2002.

Plant, W.J., P.H. Dahl, J.P. Giovanangeli, H. Branger, Bound and Free Surface Waves in a Large Wind-Wave Tank, J. Geophys. Res., 109, C10002, doi:10.1029/2004JC002342, 2004.

Plant, W.J., W.C. Keller, and K. Hayes, Simultaneous measurement of ocean winds and waves with an airborne coherent real aperture radar, J. Atmos. Ocean. Tech., 22, 832-846, doi: 10.1175/JTECH1724.1, 2005.

Rozenberg, A.D., M.J. Ritter, W.K. Melville, C.C. Gottschall, and A.V. Smirnov, Free and bound capillary waves as microwave scatterers: Laboratory studies, IEEE Trans. Geosci. Rem. Sen., 37(2), 1052-1064, 1999.

Sletten, M.A., J.C. West, X. Liu, J.H. Duncan, Radar investigations of breaking water waves at low grazing angles with simultaneous high-speed optical imagery, Radio Sci., 38(6), 1110, doi:10:1029/2002RS002716, 2003.

Trizna, D.B. and D.J. Carlson, Studies of dual polarized low grazing angle radar sea scatter in nearshore regions, IEEE Trans. Geosci. Rem. Sensing, 34(3), 747-757, 1996.

Trizna, D.B., A model for Brewster angle damping and multipath effects on the microwave radar sea echo at low grazing angles, IEEE Trans. GeoSci. Rem. Sens., 35(5), 1232-1244, 1997.

Voronovich, A.G., Small-slope approximation in wave scattering by rough surfaces, Sov. Phys. JETP, 62(1), 65-70, 1985.

Wetzel, L., On Microwave scattering by breaking waves, Wave Dynamics and Radio Probing of the Ocean Surface, K. Hasselmann and O.M. Phillips, Eds., Plenum Press, 273-284, 1986.

Wiltse, J.C., S.Pl. Schlesinger, and C.M. Johnson, Backscatering characterists of the sea in the region from 10 to 50 kMc, Proc. IRE, 45, 220-228, 1957.

Wright, J.W., A new model for sea clutter, IEEE Trans. Ant. Prop., AP-16, 217-223, 1968.

The Normalized Radar Cross Section of the Sea for Backscatter: Part 2. Modulation by Internal Waves

William J. Plant, William C. Keller, Kenneth Hayes, Gene Chatham, Brad Bell, and Nicholas Lederer
Applied Physics Laboratory, University of Washington, Seattle, WA, USA
plant@apl.washington.edu

We report measurements of the surface signatures of internal waves with dual-polarized, coherent, X-band radars mounted on three different ships and an airplane. Two sets of shipboard measurements were made in the South China Sea while the airborne data and the third set of shipboard data were collected in the Atlantic Ocean off the New Jersey coast. In the shipboard measurements in the South China Sea, internal waves generally increased the backscattering cross section near the peaks of the internal waves with no detectable decrease afterward. A very few times, however, the signatures did show increases followed by decreases in cross section. The peak of the cross section signature shifted its location relative to the internal wave crest depending on the maximum strain rate of the internal wave. In the shipboard measurements off the New Jersey coast, the range resolution of the radar was sufficiently small to allow us to detect significant modulations of surface waves on the order of 15 to 30 meters long by the internal waves. On one low-wind-speed day, simultaneous and collocated airborne and shipboard measurements were obtained off the New Jersey coast. Significant differences were seen between internal wave signatures at the very high incidence angles of the shipboard measurements and those at the moderate incidence angles of the airborne data. At the high incidence angles, the cross section for horizontally polarized transmit and receive signals, $\sigma_o(HH)$, regularly exceeded that for vertically polarized transmit and receive signals, $\sigma_o(VV)$, near the internal wave crest by 5 to 15 dB. At the more moderate incidence angles observed from the aircraft, maximum values of $\sigma_o(HH)$ and $\sigma_o(VV)$ are more nearly equal, with $\sigma_o(HH)$ often being comparable to $\sigma_o(VV)$ and only occasionally exceeding it. The intensity of modulation of the cross section caused by internal waves observed from the plane depended little on the direction of observation. In all cases, internal wave surface signatures became less visible with increasing wind speed, being very difficult to observe at 9 m/s.

Introduction

When internal waves propagate on density interfaces below the ocean surface, they produce surface currents that modulate surface waves, thus producing detectable signatures in microwave backscatter from the surface. These signatures are easily observed by synthetic aperture radar and a very large number of images of internal wave surface signatures have been obtained from orbiting spacecraft (Apel, 2004, Liu et al., 2008). Recently, sea return to shipboard radars has begun to be recorded and internal wave surface signatures in this return have been examined (Liu, et al., 2008, Chang et al., 2008).

Studies aimed at understanding the mechanisms by which internal waves modulate surface waves to produce microwave signatures have been carried out over many years.

Among the experimental studies are the seminal observations of Apel et al. (1975) from the Earth Resources Technology satellite, the 1972 work of Hughes and Grant (1978), the 1983 Joint Canada-US Ocean Wave Investigation Project (JOWIP, also called the Georgia Straits experiment) (Hughes and Dawson, 1988), the 1984 SAR Internal Wave Signature Experiment (SARSEX) (Hughes and Gasparovic, 1988), the 1987 Lock Linnhe experiment (Hogan et al., 1996), and the 1995 Coastal Ocean Probing Experiment (COPE) (Kropfli et al., 1999).   Theoretical studies into the generation of internal wave microwave surface signatures include Alpers (1985), Lyzenga and Bennett (1988), Thompson, 1988, and Kudryavtsev et al. (2005).

   Nevertheless, significant gaps still exist in our understanding of how the surface currents associated with internal waves generate the signatures observed in microwave backscatter. While the role of surface current gradients in straining surface waves is clear, it is still not known how often these current gradients simply modulate surface waves and how often they cause surface waves to break thus generating the short microwave scattering elements on the surface. Because both transmitting and receiving a horizontally polarized microwave signal (HH backscatter) causes sea return to be more sensitive to breaking surface waves than transmitting and receiving vertically polarized signals (VV backscatter), comparison of internal wave signatures at the two polarizations offers the possibility of investigating the prevalence of breaking waves in the signatures (Plant, 1997; Liu et al., 1998; Hwang et al., 2008). Unfortunately, very little work has been done in which HH and VV polarized signals have been used at nearly the same time to observe internal wave signatures, especially at moderate incidence angles (Kropfli, 1999; Churyumov, 2002). Even less work has been done to produce well-calibrated NRCS values near internal waves. Similarly, the determination of the dependence of the microwave signatures on azimuth angle has been little studied. Finally, in most situations, it is difficult to determine precisely the location of the surface signature with respect to an internal wave crest.

   In this paper, we address these issues. We report the effect of internal waves (IWs) on the normalized radar cross section of the sea, NRCS or σ_o, and on the surface velocity, which for microwaves is really the velocity of the scatterers of the microwave radiation. All measurements reported here were made with HH and VV returns measured within seconds of each other (although in one experiment a switch failed so we only obtained VV signals) and all NRCS values are calibrated. While the shipboard measurements were generally made with the radar antennas looking either in the direction of internal wave propagation or against it, the aircraft measurements were made at many different azimuth angles so the dependence of signature intensities on antenna look direction could be studied. Finally, by comparing the shipboard radar measurements with currents measured simultaneously by acoustic Doppler current profilers (ADCPs) on the same ships, the location of the surface signature relative to IW crests could be determined.

   Because our measurements were made both in the South China Sea and in the Atlantic Ocean off the New Jersey coast, two very different types of internal waves were studied. In the South China Sea, surface signatures of very non-linear internal solitons, which traveled in widely spaced trains, were observed. We also found that in the South China Sea, regular nearly sinusoidal trains of smaller amplitude internal waves were very frequently observed. These smaller waves were very similar to the internal waves

encountered off the New Jersey coast. We first discuss signatures of the non-linear solitons then the smaller sinusoidal wave trains.

Shipboard Measurements in the South China Sea

   Two sets of shipboard measurements were made in the South China Sea. In 2005, our X-band, coherent radar called RiverRad was mounted on the R/V Revelle and took measurements in the South China Sea from April 18 to May 14. These measurements were all taken in deep water. In 2007, we operated RiverRad on two cruises, one from April 24 to May 13 was in the relatively shallow water of the western shelf of the South China Sea while the second from May 13 to May 20 was in deep water. On all these cruises, the parabolic, pencil-beam antennas were pointed approximately in the direction of the ship's heading. Figure 1 shows RiverRad mounted on these two ships while Figure 2 indicates where in the South China Sea significant non-linear solitons were encountered.

Figure 1. a) The parabolic antennas of RiverRad are seen mounted on the R/V Revelle in 2005. b) RiverRad mounted on the Taiwanese ship R/V Ocean Researcher 1 in 2007.
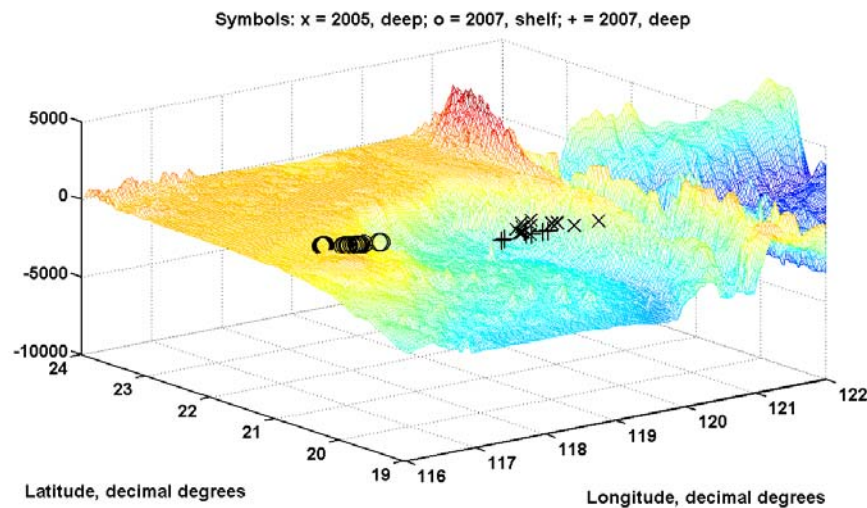

Figure 2. Locations at which non-linear internal solitons were encountered in the South China Sea. Shallow water, 2007 – circles; deep water, 2007 - +; deep water, 2005 – X.

Figure 3 shows the types of data collected on these cruises. The standard shipboard measurements of wind speed and direction, ship speed and direction, and currents from ADCPs were collected and recorded. From the latter measurements, currents were extracted from the nearest good bin to the surface and resolved into components in and perpendicular to the ship heading as shown in the third panel from the top of Figure 3. In 2005, the nearest good bin to the surface was 17 m below the surface; in 2007, it was 52 m deep. In addition, latitude, longitude, time, pitch, and roll were recorded during the cruise. The latter two variables were used in correcting the incidence angle of the radar for ship motion. We also had a GPS receiver mounted on the RiverRad antennas and its speed readings were used to correct the Doppler shifts observed by RiverRad. In addition to the ship speed from the GPS shown in Figure 3, the speed indicated by a pitot tube on the ship's hull was recorded. The difference between the two measured speeds was another measure of current in the heading direction.
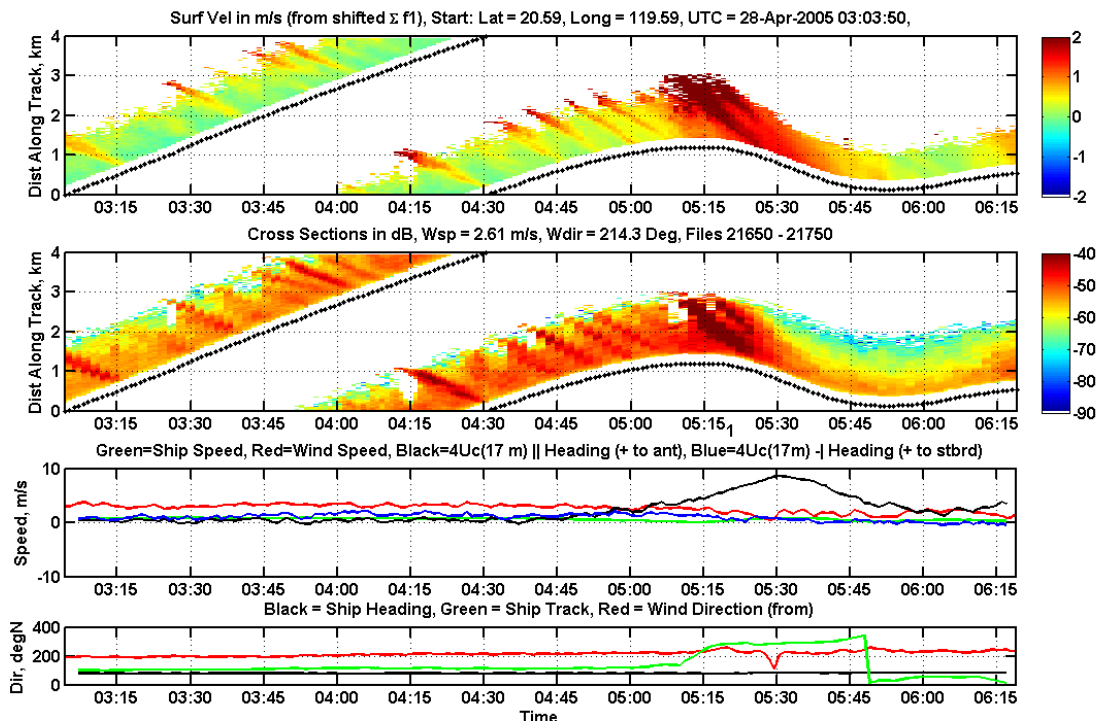

Figure 3. An example of data collected from the R/V Revelle in 2005 averaged over 50 sec. The top panel shows radar surface (scatterer) velocities in the direction of the ship's heading as functions of distance in the heading direction and time. Distances are wrapped at 4 km. The curve of black dots is the ship's location. The second panel down shows a similar plot of normalized radar cross section in the direction of the ship's heading. The microwave measurements were made only at VV polarization in 2005. The third panel down shows the ship speed in green, the wind speed in red, four times the ADCP current at 17 m depth along (black) and perpendicular (blue) to the ship's heading. Currents in the heading direction are positive if they come toward the ship and currents perpendicular to the heading are positive to starboard. Finally the bottom panel shows

compass readings of the ship's heading (black), ship track (green), and wind direction (from, red).

Microwave data consisted of the standard output of RiverRad, which has been described previously elsewhere (Plant, 2005b). Briefly, RiverRad is a coherent, 9.36 GHz radar that receives signals from a series of range bins sufficiently rapidly to calculate a Doppler spectrum at every bin. Averages of these spectra over a complete record were stored for each range bin. In 2005 a record was 50 seconds long, in 2007 it was 30 minutes long. In addition, the first three moments of the Doppler spectrum, mean power, Doppler offset, and Doppler bandwidth are stored for every scan, each of which was a approximately 365 msec long. Alternate scans were collected with HH and VV polarizations. Therefore a scan at each polarization was 365 msec long and scans occurred every 730 msec. The range resolution was 15 m.

From the three recorded moments of the spectrum, we obtained the normalized radar cross section (NRCS or σ_o, a measure of surface roughness), the mean surface velocity, and the spread in scatterer velocities for each range bin averaged over a scan time (365 msec). Images of the surface velocity are shown in the top panel of Figure 3 while images of σ_o are shown in the second panel from the top. These images are space-time plots of the return to the radar along the antenna-look direction, the direction of the ship's heading. They were smoothed over 50 sec. The swaths wrap from top to bottom at 4 km so the vertical axis is distance along the ship's heading from the start of the run, modulo 4. The black dotted curves in the images show the location of the ship. The radar return starts about 250 m in front of the ship and goes out to almost 2 km. The antennas were 18 m above the water surface so the incidence angle ranged from 85.9^o to 89.5^o. Note that this type of display places the radar return at the location it has for a stationary observer if the ship's heading is constant.

Surface signatures of two types of internal waves, small nearly sinusoidal waves and a larger soliton wave, are clearly present in both the velocity and cross section measured by the radar. As indicated by the sign of the ADCP-measured internal soliton current along the heading and the lack of internal soliton current perpendicular to the heading, the ship was travelling directly opposite the direction of propagation of the large internal wave. The train of smaller sinusoidal internal waves with a wavelength of less than 800 m is observed in both the surface currents and cross sections in front of the large soliton. Both the surface velocity and the cross section of the smaller waves increase significantly over the large internal wave. Apparently the interaction of the soliton and the smaller wave train increases the amplitude of the small wave train. In fact the small wave train is difficult to observe after the ship has passed the soliton, indicating that it may have been blocked by the soliton.

The slope of these surface features is the speed of the internal wave if the perpendicular ADCP current is zero. If the internal waves do not propagate directly toward or away from the radar, then the slope of the feature is the maximum possible speed of the internal wave. The train of small internal waves is clearly visible in the radar return but is barely visible in the currents measured at 17 m depth. This makes it difficult to determine their direction of propagation except that a component of their propagation vector comes toward the ship because the slope is negative. We can say with

certainty that the train of small internal waves is moving much more slowly than the soliton. Furthermore, their speed is increasing as they approach the crest of the soliton.

In order to obtain the precise location of the increases in cross section and surface velocity caused by the soliton with respect to the location of the soliton, their effects must be extrapolated to the position of the ship. Carrying out this extrapolation in the images of Figure 3, clearly shows that the surface signature of the internal wave, in both cross section and velocity is nearly directly above the soliton crest. As we will show later, we generally found that in deep water, the surface signature maximized near the crest of the internal wave.

Figure 4 shows that the signature does not always maximize directly above the soliton. The data shown in this figure are from the 2007 cruise on the OR1 in shallow water. The format of this figure is the same as that of Figure 3. Again, the ship travels very nearly opposite the direction of soliton movement. Now, however, maxima in both the cross section and surface velocity signatures of the wave occur well before the crest of the soliton reaches the ship.
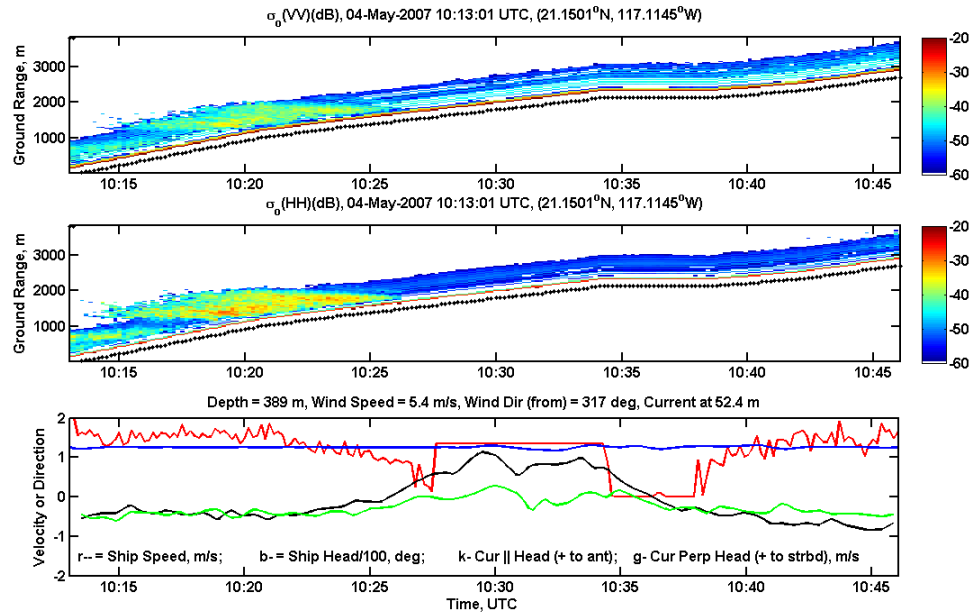

Figure 4. Data from the 2007 cruise of the OR1 on the shelf of the South China Sea. The format is the same as that of Figure 3.

Figure 5 summarizes the location of the maximum cross section with respect to soliton wave crests for all of the data we collected in 2005 and 2007. The figure plots the distance by which the signature maximum leads the wave crest versus the maximum current produced by the wave at 17 or 53 m depth, both normalized by the width of the wave. The definition of width was taken to be the full width at half the maximum current. The figure shows that the signature of the soliton occurs farther in front of the crest the steeper the wave is. In general solitons in the shallow water of the shelf are steeper than in deep water and their signature leads the soliton crest by greater distances. In only one case, the x enclosed in a diamond, did this behavior not occur.

In the vast majority of cases that we examined, the response of the cross section to the surface currents set up by the internal waves was an increase unaccompanied by any significant decrease. The symbols in Figure 5 that are enclosed in squares show the cases where this was not true and the increase was followed by a significant decrease. We do not believe that the behavior of the majority of our data is due to the fact that a decrease in cross section is hidden by noise as suggested by da Silva et al. (1998) for SAR imagery
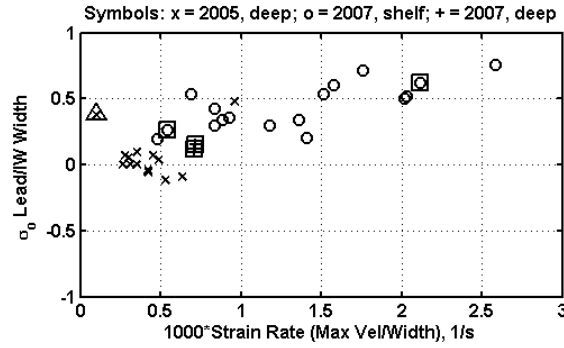

Figure 5. Distance by which the maximum cross section leads the internal wave crest as a fraction of the width of the wave versus the maximum current set up by the internal wave divided by the width of the wave, a measure of the maximum strain rate. Symbols with squares or a diamond around them are discussed in the text.
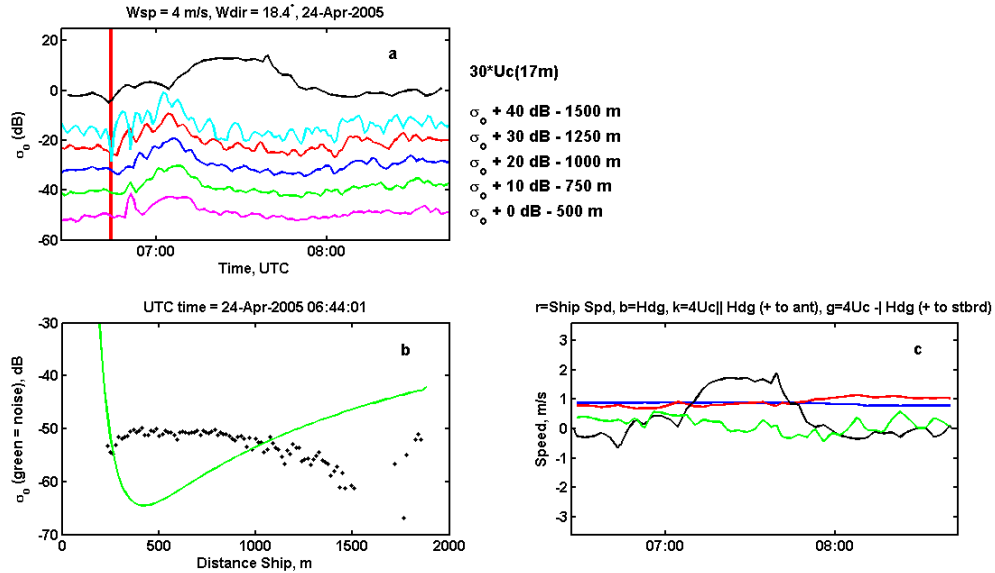

Figure 6. a) Colored curves show the NRCS measured at various ranges as a function of time. NRCS values at different ranges are offset as indicated in the figure. The black curve is 30 times the ADCP current in the heading direction. b) Black symbols show the range dependence of the NRCS measured at the time indicated by the vertical red line in a. The green curve shows the noise level of the radar. c) The red curve is ship speed, the blue curve is ship heading divided by 100, the black curve is four times the ADCP current in the heading direction, and the green curve is the ADCP current perpendicular to the heading.
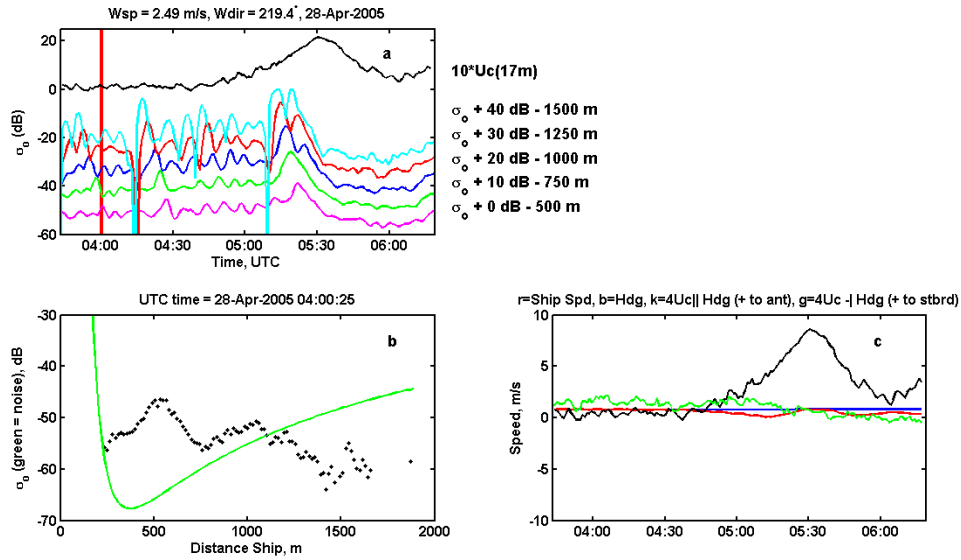
Figure 7. Same as Figure 6 but for April 28, 2005, illustrating a case where an internal wave caused an NRCS increase followed by a decrease.
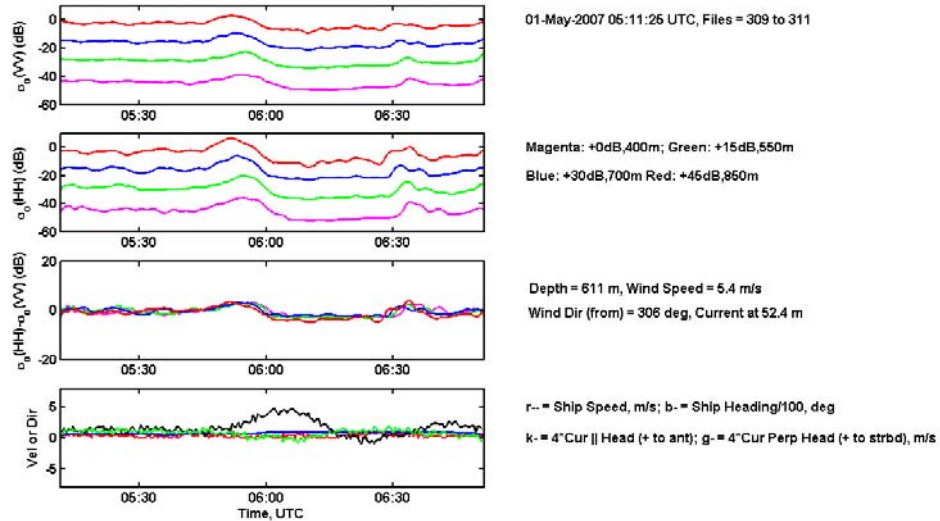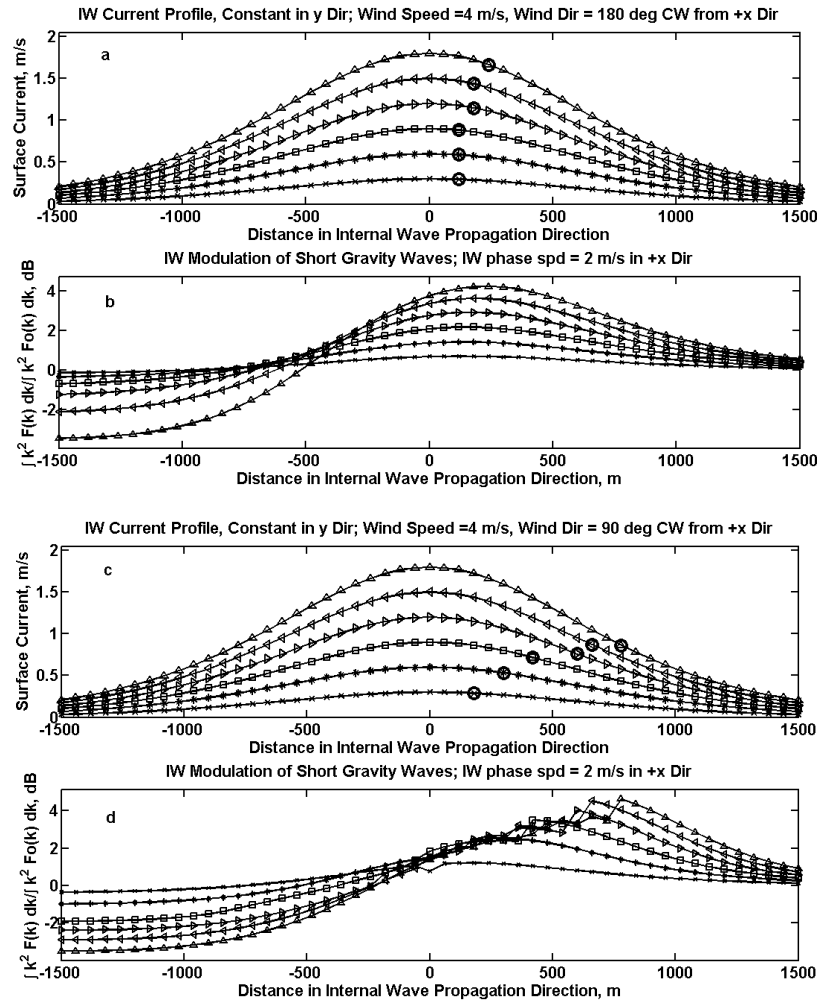

Figure 8. Illustration of two sequential internal wave causing different responses in the NRCS. The top panel is a time series of VV NRCS values at various ranges as the internal solitons are crossed. The second panel from the top is a similar plot for HH polarization. In both these panels, NRCS values are offset at various ranges as shown on the figure. The third panel from the top gives the polarization ratios at various ranges without offsets. The bottom panel shows the ship speed in red, the ship heading divided by 100 in blue, the along-heading ADCP current times four in black, and the cross-heading ADCP current in green.

of internal waves. Figure 6 illustrates that RiverRad's signals are generally well above the noise level. Two of the cases where increases were followed by decreases are illustrated in Figures 7 and 8. Figure 7 is in the same format as Figure 6 and shows an NRCS increase followed by a decrease. Note the presence of small nearly sinusoidal

waves before the internal soliton arrives at the ship and their absence afterward. Figure 8 illustrates a case from 2007 where the sinusoidal waves are not so prominent. Note that the increase/decrease occurs for both HH and VV polarizations for the first internal wave but does not occur for either when the second internal wave arrives. For both internal waves, the polarization ratio exceeds 0 dB at its maximum value.

We have compared these observations with the output of the standard action balance model of short wave modulation by internal wave currents (Thompson and Gasparovic, 1986; Thompson, 1988; Lyzenga and Bennett, 1988; Kudryatsev et al., 2005). Most researchers agree that the direct modulation of centimeter-length Bragg scatterers by the internal wave surface currents is very small. Therefore the consensus is that intermediate-scale waves are modulated by the internal wave currents and that at the location where these maximize, the modulation of centimetric wind waves or the generation of small-scale roughness by breaking will also maximize. Thus for the purposes of our comparison, we looked at the modulation of the mean-square slope of waves between 24 cm and 6.67 m long. We computed using the action balance techniques outlined by Lyzenga and Bennett (1988) the relative modulation of these waves by internal solitons of fixed width but of variable amplitude. We did this for three different wind directions relative to the internal wave propagation direction, 0°, 90°, and 180°. The results are shown in Figure 9.

IW Current Profile, Constant in y Dir; Wind Speed =4 m/s, Wind Dir = 0 deg CW from +x Dir

IW Modulation of Short Gravity Waves; IW phase spd = 2 m/s in +x Dir
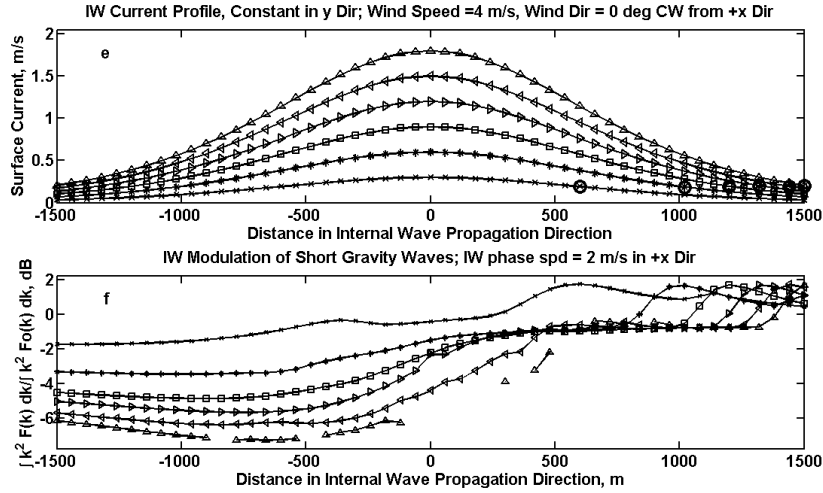
Figure 9. a) Surface currents for internal waves of six different amplitudes with the positions of the maximum mean square slope of short gravity waves between 24 and 667 cm long as predicted by action balance equations shown as circles. b) Mean-square slope of short gravity waves relative to the mean-square slope of a wave field undisturbed by IW currents for the six different solitary wave currents shown in a. In a and b, the 4 m/s wind blows opposite the IW propagation direction. c) Same as a but wind now blows perpendicular to the IW propagation direction. d) Same as b but wind now blows perpendicular to the IW. e) Same as a but wind now blows in the direction of the IW propagation direction. f) Same as b but wind now blows in the direction of the IW propagation direction.

We found that when the wind blew against the internal wave (Figures 9a and b), the maximum modulation moved down the forward face of the internal wave as its amplitude increased but by much smaller distances than we observed. When the wind blew perpendicular to the internal wave (Figures 9c and d), the maximum modulation moved much more in line with our observations. When the wind blew in the direction of the internal wave, the maximum modulation moved down the forward face of the internal wave somewhat farther than the majority of our measurements did (Figures 9e and f). Figure 10 shows histograms of wind speeds and directions relative to the IW propagation directions for the times of our measurements.

For all three of the wind directions that we modeled, a depression of the relative modulation occurred behind the crest of the internal wave. This depression was generally small for low-amplitude internal waves but became larger as the internal wave steepness increased. Our data do not support the idea of a large decrease of NRCS being associated with large internal wave steepnesses (see Figure 5). Nevertheless, the small decreases associated with smaller amplitude internal solitons may explain why we generally did not observe decreased NRCS associated with the surface signatures. If the decrease was as small as the calculations suggest, we may not have been able to detect it.
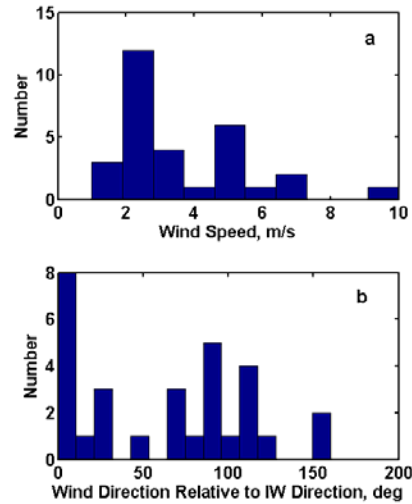
Figure 10. a) Histogram of wind speeds during measurements of internal waves. b) Histogram of wind directions relative to the IW propagation direction during the same measurements.

Airborne and Shipboard Measurements off the New Jersey Coast

Measurements in the Atlantic Ocean near the New Jersey shelf break were made both on the R/V Endeavor and on a Cessna Skymaster. Figure 11 shows RiverRad mounted on the ship (left) and a similar coherent radar, CORAR, mounted on the plane (right).

For the shipboard measurements, RiverRad's antennas were scanned back and forth in a windshield-wiper fashon through an arc 80° in azimuth centered at 24° higher azimuth angle than the heading. The antennas were mounted 35° apart in azimuth; one was VV polarized and the other was HH polarized. The VV antenna was at the higher azimuth angle. The antennas swept through their 80° arc in approximately 40 seconds. The range resolution was set to 3.75 m.

The airborne measurements were made in a side-looking mode. The VV and HH antennas were mounted one above the other looking to the left side of the plane. CORAR has been described in detail by Plant et al., 2005a. CORAR is very similar to RiverRad

Figure 11. Left: RiverRad mounted the R/V Endeavor in 2006. Right: CORAR mounted on the Cessna Skymaster at the same time.

except that data are collected and stored more quickly as is necessary for airborne operation. A scan was 340 msec in length and the first three spectral moments were saved at every range bin on each scan along with a complete spectrum from a selected range bin.

Figure 12 shows an image of internal waves from the shipboard data collected on the Endeavor. The top row shows cross sections at HH (left) and VV (right) polarizations while the bottom row shows the corresponding scatterer velocities. Clearly $\sigma_o(HH)$ is much larger than $\sigma_o(VV)$ near the crests of the internal waves. Similarly scatterer velocities are much larger for HH polarization than for VV. Velocities at HH frequently exceed 1 m/s, sometimes reaching 2 to 3 m/s. Similarly high velocities can be seen in the VV image though velocities in general are much lower at this polarization. We interpret these results as being evidence of the involvement of breaking waves in microwave signatures of internal waves.
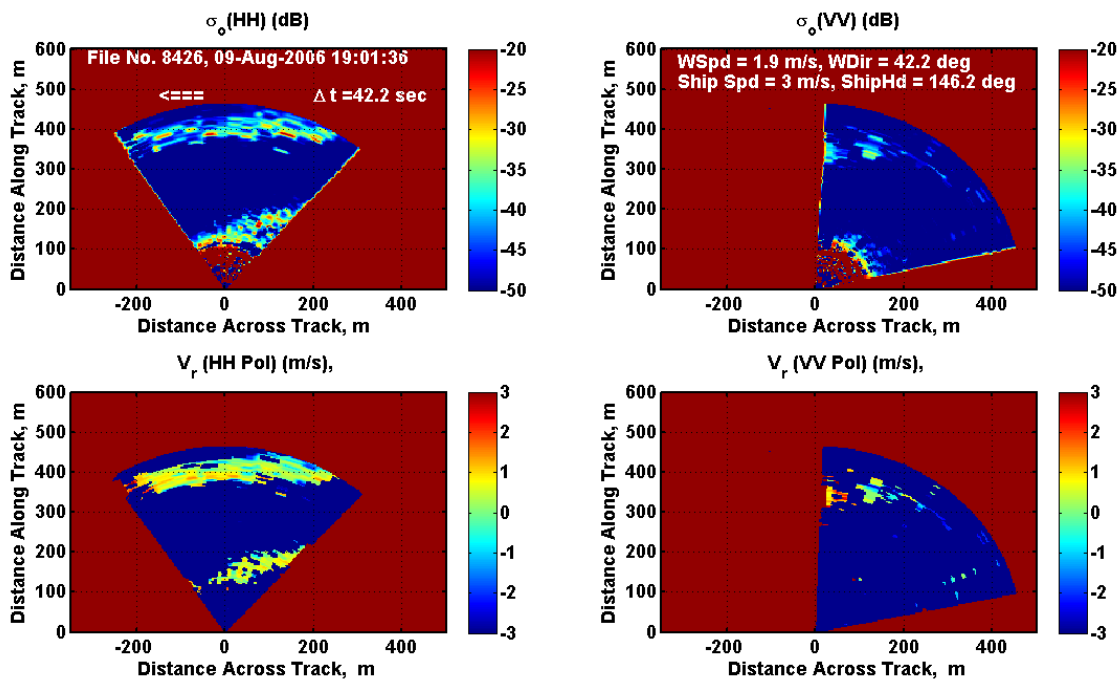

Figure 12. Images of internal waves collected in 2006 from the R/V Endeavor. The top row shows $\sigma_o(HH)$ (left) and $\sigma_o(VV)$ (right); the bottom row shows scatterer velocities at HH (left) and VV (right). Normalized radar cross section scales are in dB; velocity scales are in m/s. Positive velocities are toward the radar. Dark blue in the bottom row indicates that the signal-to-noise ratio was too low to determine a velocity.

Unfortunately, we were unable to determine the phase of the microwave signatures with respect to the surface velocities set up by the internal waves for these shipboard measurements because the radar measurements and the ADCP measurements did not overlap. The radar operated early in the experiment until a large storm damaged the antennas and the ADCP did not begin operating until after this storm.

One striking feature of the images shown in Figure 12 is that both the cross sections and velocities are highly variable within the area of strong return. If we average the data in these images that are within 20° of the ship's heading, we obtain plots as a function of ground range such as those shown in Figure 13. For the three different times shown in

Figure 13, the ship was always heading into the internal waves and the antennas were always rotating counterclockwise. Thus the VV antenna viewed the heading direction about 20 seconds later than the HH antenna and the figure shows that the internal wave has advanced (moved left) during that time. This motion includes both the IW speed and the ship speed. All of the panels of Figure 13 show indications of oscillations of length 15 to 30 meters. For the HH return, though, these oscillations increase significantly on the forward face of the general increase in cross section due to the internal waves. The internal wave increases the amplitude of these short gravity waves, leading to an oscillating cross section. The differences between the ship's heading and the wind direction in the three cases shown are 104°, 74°, and 118°. Thus, the wind is almost perpendicular to the internal wave in all cases so a significant increase in short gravity waves is expected in front of the crest of the internal wave as shown in Figure 9d. The increase in these waves affects the HH cross section more than the VV cross section.
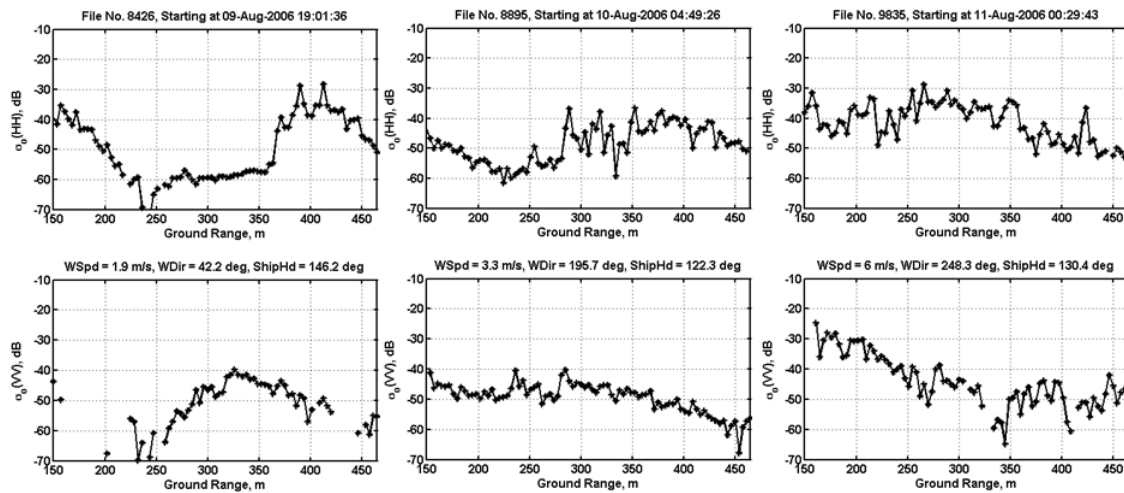

Figure 13. Average cross section versus ground range for data taken within 20° of the ship's heading. The top row plots $\sigma_o(HH)$ as a function of ground range at various times while the bottom row shows similar plots of $\sigma_o(VV)$ at the times that are a few minutes different.

The airborne imagery also confirms the fact that HH cross sections are more affected by internal waves than VV. Figure 14 documents one case of a flight track across a train of internal waves. Internal-wave-induced oscillations in the HH imagery are much more pronounced than in the VV imagery even though the mean cross section level in the VV image exceeds that in the HH image. This is also obvious in the ratio of the standard deviation to mean cross section also shown in the figure. Figure 15 shows the same data with the mean cross section level removed to emphasize the higher modulation at HH polarization. Spectra of the images in Figures 15a and b are shown in Figures 15c and d. We will use below two measures of both the internal wave propagation direction and the intensity of its surface signature. Directions can be obtained both from the imagery and from the spectra. The intensity of the surface signature is given both by the ratio of standard deviation to mean cross section of Figure 14 and by the rms level of the image spectra that are shown in Figures 15c and d.
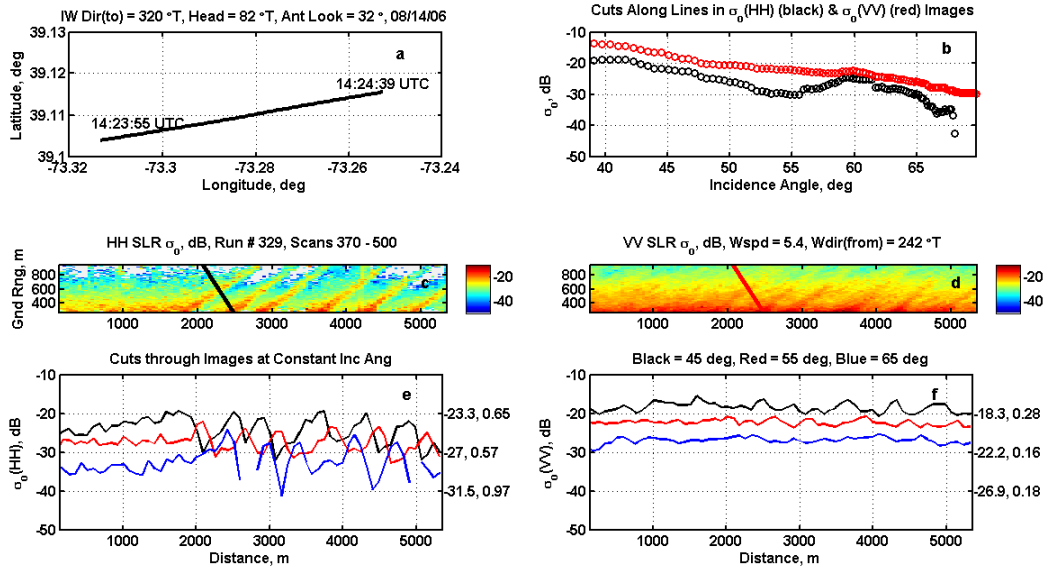
Figure 14. a) Track of the Skymaster. b) Normalized radar cross sections versus incidence angle along the lines in panels c and d. c) Image of σ_o(HH). d) Image of σ_o(VV). e) Cuts through σ_o(HH) image at constant incidence angles of 45°, 55°, and 65°. The numbers to the right are mean cross section and its standard deviation divided by the mean at the three incidence angles. f) Same as e but for σ_o(VV) .
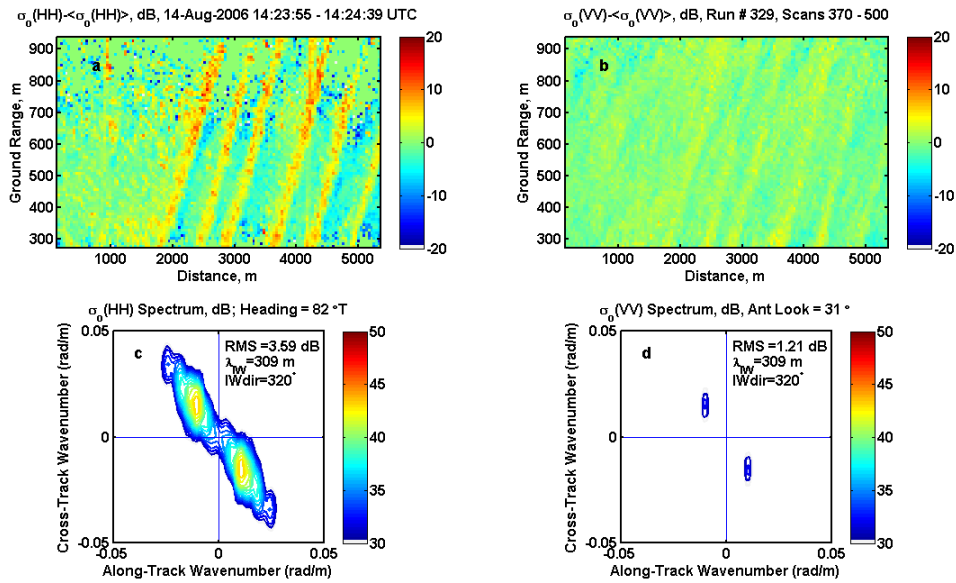

Figure 15. a) Zero-mean image of σ_o(HH). b) Same as a but for σ_o(VV). c) Spectrum of zero-image of σ_o(HH). Aircraft heading is shown above the spectrum and the rms value of the spectrum, the wavelength of the IW, and its direction of propagation in degT are also shown. d) Same as c but for σ_o(VV). The direction of the antenna look relative to the internal wave propagation direction is shown above the image.

On August 9, 2006, the plane and the ship both traversed the same internal wave train many times. The ship travelled either against the internal wave or with it but the plane flew in many different compass directions. We were therefore able to determine the maximum NRCS produced by the internal wave looking both upwave and downwave at a variety of incidence angles. From the plane measurements, we could also determine the dependence of the internal wave signature on antenna look direction. Figure 16 shows the average of the maximum NRCS values for both HH and VV polarizations produced by the internal waves when the antennas looked upwave (right) and downwave (left). Also shown in this figure are the crosswind NRCS values predicted by the multiscale model (Plant, 2002) for a sea surface disturbed only by the wind. These curves are the same in the left and right columns since these columns are the same in the absence of internal waves. We have not shown multiscale predictions for the panels where the wind speed is between 1 and 2 m/s since at these low winds, model predictions depend not only on the wind speed but also on its variability. This latter quantity was difficult to estimate.
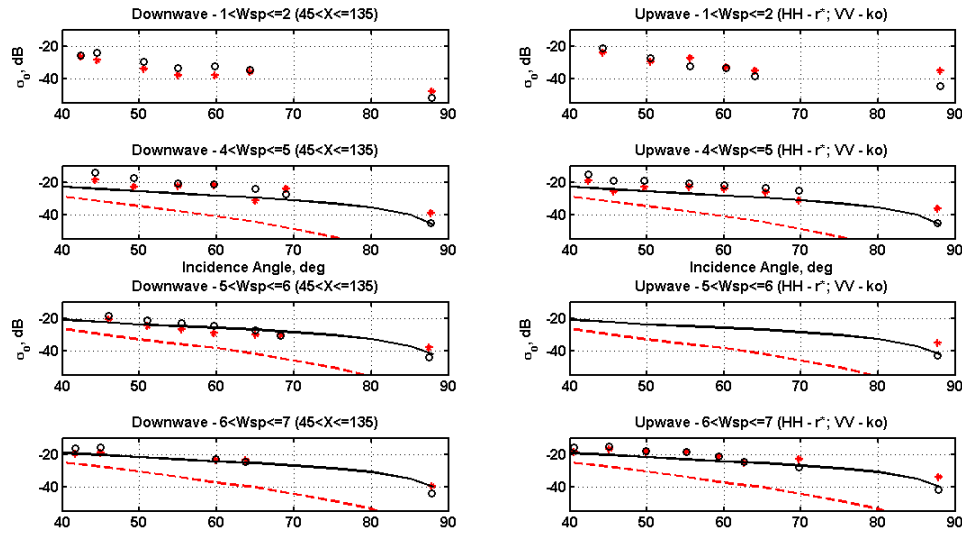

Figure 16. Maximum NRCS values of the microwave signature of an internal-wave train as a function of incidence angle. Data in the left column were collected when the antennas looked along the internal wave's propagation direction; data in the right column were obtained with the antenna looking into the internal wave. The lines are predictions of the multiscale model of Plant (2002) for a sea surface disturbed only by wind averaged over azimuth angles between 45° and 135°. Black lines and circles refer to VV polarization; red dashed lines and asterisks refer to HH.

Figure 16 suggests several conclusions. Clearly, maximum σ_o values of internal wave signatures are much closer to multiscale predictions at VV polarization than at HH. This agrees with the less distinct internal wave signatures at VV than at HH that we have pointed out above. There is some tendency for maximum $\sigma_o(VV)$ to trend closer to the multiscale predictions at higher wind speeds and incidence angles. This suggests that internal wave signatures at VV polarization should be relatively difficult to detect under these circumstances. Maximum $\sigma_o(HH)$ values of internal wave signatures are much higher than the values predicted by the multiscale model. This model does not include

wave breaking and we believe that breaking waves are the most likely source of the enhanced backscatter at HH polarization at the maxima of the internal wave signatures. This interpretation is supported by the observation that in the shipboard data, σ_o(HH) is 5 to 10 dB higher than σ_o(VV). We cannot rule out the possibility that wave breaking also plays a role in increasing σ_o(VV) at signature maxima above its predicted value at low wind speeds.

The flights of the Skymaster over all internal waves we viewed near the shelf break showed that there is very little tendency for the signature of the internal waves to vary depending on antenna look direction at moderate incidence angles. Figure 17 documents this. Ratios of the standard deviation to the mean cross section over the internal wave and the rms value of the image spectrum are shown in this figure. In all cases, no dependence of the signature on azimuth angle can be detected. Note once again that internal wave signatures are more distinct in HH backscatter than in VV.
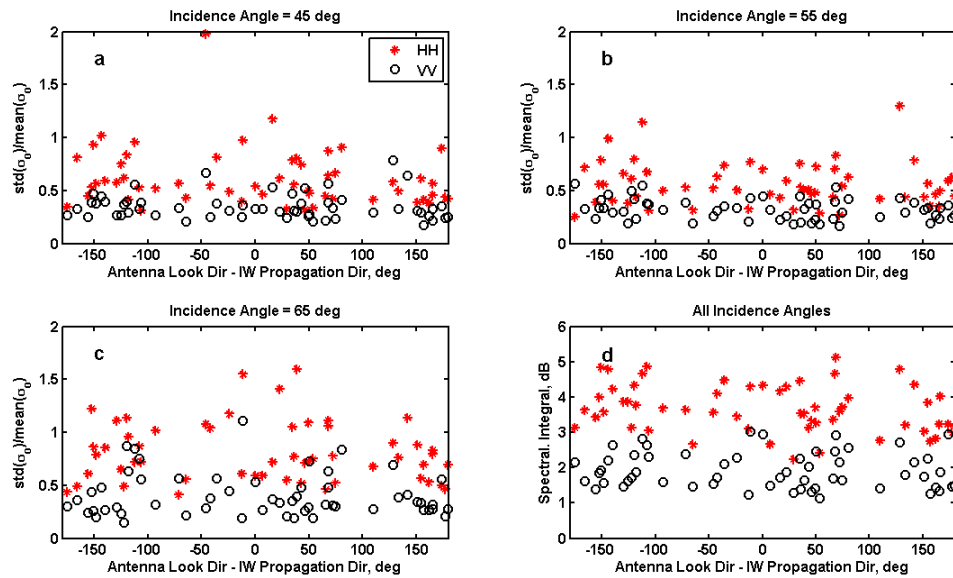

Figure 17. Measurements of the intensity of the internal-wave microwave signature for various antenna look directions. a) The ratio of the standard deviation to the mean cross section of the IW train at an incidence angle of 45°. b) Same as a but for a 55° incidence angle. c) Same as a but for a 65° incidence angle. d) The rms value of the image spectrum. This is necessarily calculated over the range of incidence angles that formed the image.

Finally, in Figure 18, we show these same measures of intensity as a function of wind speed for all the data that we collected from the plane. As is well known, IW signatures become less distinct as the wind speed increases and Figure 18 indicates this. We find that the signatures have nearly disappeared at a wind speed of 9 m/s.
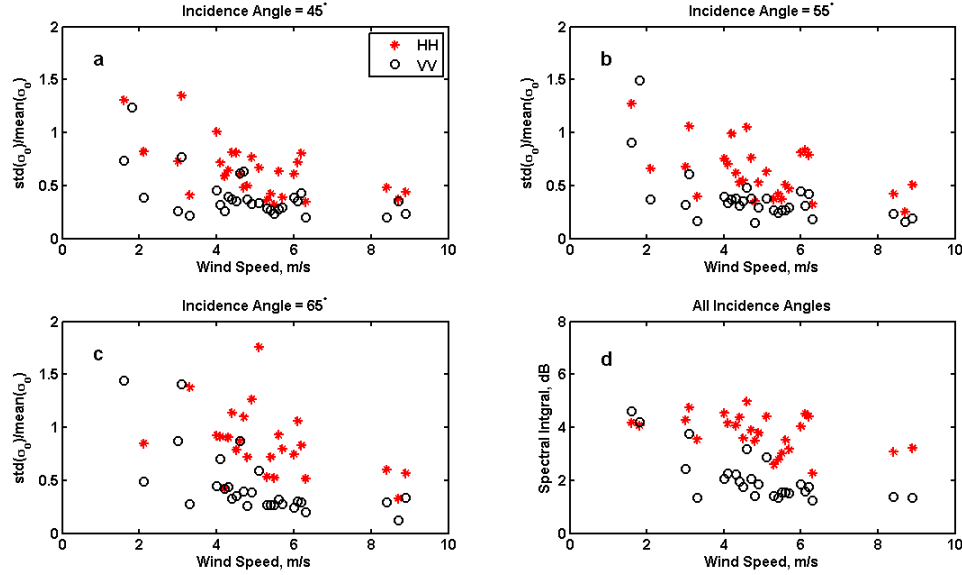
Figure 18. Dependence of the intensity of internal wave signatures on wind speed. The various panels show the same dependent variables as Figure 16.

Conclusions

We have shown not only that microwave signatures of internal waves are more distinct at HH polarization than at VV but also that maximum σ_o(HH) values are comparable to or even greater than maximum σ_o(VV) values induced by the internal waves. The maximum σ_o(HH) values produced by internal wave surface disturbances are much larger than the multiscale model predicts while maximum σ_o(VV) values are comparable to or above the predicted values. Furthermore, the intensities of the signatures at both polarizations vary little with the direction of antenna look. All of these results suggest to us that breaking waves play a significant role in the production of microwave signatures by internal waves. The many ways that this could happen were outlined in Part 1.

The cross section maximum of the signature leads the maximum near-surface velocity of the internal wave by larger distances the steeper the internal wave is. This same behavior is seen in simulations of the location of the maximum modulation of short gravity waves by internal waves using standard action balance techniques. This strongly suggests that microwave signatures of large internal waves are produced by the breaking of short gravity waves as they are modulated by the internal waves. In fact, in our shipboard measurements off the New Jersey coast, we observed cross section oscillations 15 to 30 meters in length that were modulated by the internal waves.

Most of the microwave signatures observed in this low-grazing-angle study consisted of increases of the microwave cross section by the internal waves. A few observations of increases followed by decreases were also recorded. We did not observe cases consisting only of a decreased cross section. We note that our simulations of short gravity wave modulation by internal waves also showed cases of both increases and increases followed by decreases in the modulation intensity. Da Silva et al. (1998) have reported seeing

microwave surface signatures of internal waves from satellites at much higher grazing angles that consisted of cross section increases, decreases, and paired increases and decreases. They associated the first type of signature with low-wind conditions where the decrease is not visible due to system noise. This was not the case in our low-grazing-angle study. Our signal-to-noise ratio was sufficiently high that decreased cross sections were not hidden by noise.

The movement of the intensity maximum down the front face of the internal soliton as the wave steepened probably explains the results of Kropfli et al. (1999) that NRCS maxima in sinusoidal internal waves trains lie near the minima of the surface currents generated by the IW. Their quoted IW phase speeds are 0.7 to 0.9 m/s while the maximum currents 4.4 m below the surface appear to be less than 0.7 m/s and the time required for an IW to pass a fixed point is about 0.1 hours (full width at half max). Thus one thousand times the ratio of surface current to width, a measure of maximum strain rate, is about 2.8 1/s or a bit higher than the highest found in this study. Since wind directions generally had a significant component perpendicular to the IW propagation direction during the study, this implies that their modulation pattern should lead the IW current by nearly the width of the internal wave putting it nearly out of phase with a sinusoidal current. We were not able to verify this for the sinusoidal waves we observed off the New Jersey coast because the radar measurements and ADCP measurements did not overlap.

Much additional information is available in this data set and is being studied. In particular, we are able to obtain the speeds of the internal waves from plots such as those shown in Figures 2 and 3. We are investigating these speeds and attempting to compare them with predicted non-linear wave speeds. Finally, we have not yet processed our data to yield the velocity spread within each range cell. This would aid in the identification of breaking-wave events and will be undertaken.

Acknowledgments

References

Alpers W., Theory of radar imaging of internal waves, Nature, 314, 245-247 1985.

Apel,J.R., H.M. Byrne, J.R. Prom, and R.L. Charnell, Observations of oceanic internal and surface waves from the Earth Resources Technology Satellite, J. Geophys. Res., 80(6), 865-881, 1975.

Apel, J.R., Oceanic Internal Waves and Solitons, in *Synthetic Aperture Radar Marine User's Manual*, edited by C.R. Jackson and J.R. Apel, pp. 189-206, U.S. Department of Commerce, 2004.

Churyumov, A.N., Yu.A. Kravtsov, O. Yu. Lavrova, K. Ts. Litovchenko, M.I. Mityagina, and K.D. Sabinin, Signatures of resonant and non-resonant scattering mechanisms on radar images of internal waves, Int. J. Rem. Sensing, 23(20), 4341–4355, 2002.

Hogan, G.G., R.D. Chapman, G. Watson, and D.R. Thompson, Observations of ship-generated internal waves in SAR images from Loch Linnhe, Scotland, and comparison with theory and in situ internal wave measurements, IEEE Trans. Geosci. and Rem. Sens., 34(2), 532-542, 1996.

Hughes, B.A., and T.W. Dawson,Joint Canada-U.S. Ocean Wave Investigation Project: An Overview of the Georgia Strait Experiment, J. Geophys. Res., 93(C10), 12219-12234, 1988.

Hughes, B.A. and R.F. Gasparovic, Introduction, J. Geophys. Res., 93(C10), 12217, 1988

Hughes B.A., H.L. Grant, Effect of internal waves on surface wind waves. 1. Experimental measurements, J. Geophys Res., 83(C1), 443-454 1978.

Hwang, P., M.A. Sletten, and J.V. Toporkov, Breaking wave contribution to low grazing angle radar backscatter from the ocean surface, J. Geophys. Res., 113, C09017, doi:10.1029/2008JC004752, 2008.

Kropfli, R.A., L.A. Ostrovski, T.P. Stanton, E.A. Skirta, A.N. Keane, and V. Irisov, Relationships between strong internal waves in the coastal zone and their radar and radiometric signatures, J. Geophys. Res., 104(C2), 3133-3148, 1999.

Kudryavtsev, V., D. Akimov, J. Johannessen, and B. Chapron, On radar imaging of current features: 1. Model and comparison with observations, J. Geophys. Res, 110, C07016, doi:10.1029/2004JC002505, 2005.

Lui, A.K., C-R. Ho, and C-T. Liu, *Satellite Remote Sensing of the South China Sea*, 312 p, Tingmao Publish Company, Taipei, Taiwan, 2008.

Liu, Y., S.J. Frasier, and R.E. McIntosh, Measurement and Classification of Low-Grazing-Angle Radar Sea Spikes, IEEE Trans. Geosci. Rem. Sensing, 46(1), 27-40, 1998.

Lyzenga D.R., J.R. Bennett, Full-spectrum modeling of synthetic aperture radar internal wave signatures, J. Geophys. Res., 93(C10), 12345-12354, 1988.

Plant, W.J., W.C. Keller, and K. Hayes, Simultaneous measurement of ocean winds and waves with an airborne coherent real aperture radar, J. Atmos. Ocean. Tech., 22, 832-846, doi: 10.1175/JTECH1724.1, 2005a.

Plant, W.J., W.C. Keller, and K. Hayes, Measurement of river surface currents with coherent microwave systems, IEEE TGRS, 43 (6), 1242-1257, doi: 10.1109/TGRS.2005b.845641, 2005b.

Thompson, D.R., and R.F. Gasparovic, Intensity modulation in SAR images of internal waves, Nature, 320, 345-348, 1986.

Thompson D.R., Calculation of radar backscatter modulations from internal waves, J. Geophys. Res., 93(C10), 12371-12380, 1988.

Outline of this paper

1. At low grazing angles, IWs always increase the cross section. (What about at mid incidence angles from aircraft? Can't tell.)

2. Polarization ratios of IW-disturbed backscatter are often greater than 1 for both airborne and shipboard measurements.

3. For shipboard measurements, maximum cross sections occur farther forward of the wave crest for steeper waves, ie, farther forward on the shelf, near peak in deep water

4. Phase speeds? Just a little so that location of cross section maxima can be determined. Will need IW widths, intensities.

5. Many different kinds of surface signatures of IWs in the South China Sea. (Small ones similar to those off the NJ coast? Next paper.

6. If possible, compare with theoretical amplitude modulations.

7. Angular dependence of IW modulation from aircraft measurements. (Need to get ADCP currents included)

Other Paper:

1. IW interactions

2. IW phase speeds versus max velocity

3. Compare with two-layer fluid theory.

4. IW widths, amplitudes

Still Another Paper (Like IGARSS10 Abstract):

1. Document environmental conditions under which breaking is important
2. Document radar conditions under which breaking is important
3. Include Doppler bandwidths in the study.